

**Behaviours of Bifilms in A356 Alloy during
Solidification: Developing Observation
Techniques with 3-D Micro X-ray Tomography**

By

Jun Mo Park

This thesis submitted to
The University of Birmingham
For the degree of
Masters of Research

School of Metallurgy and Materials
College of Engineering
The University of Birmingham
June 2009

UNIVERSITY OF
BIRMINGHAM

University of Birmingham Research Archive

e-theses repository

This unpublished thesis/dissertation is copyright of the author and/or third parties. The intellectual property rights of the author or third parties in respect of this work are as defined by The Copyright Designs and Patents Act 1988 or as modified by any successor legislation.

Any use made of information contained in this thesis/dissertation must be in accordance with that legislation and must be properly acknowledged. Further distribution or reproduction in any format is prohibited without the permission of the copyright holder.

Abstract

The reduction of mechanical properties by oxide films has been documented and studied for decades. Among these studies, Campbell proposed that tangled thin oxides created during the filling of a mould become flattened or acquire a spherical shape because of several processes: the penetration of dissolved hydrogen from the liquid aluminium into the bifilm during solidification, the pushing of oxides by dendrites during solidification, the growth of heterogeneously nucleated intermetallic faces upon the wetted oxide side, and shrinkage that pulls oxides. This proposal has been argued from a theoretical standpoint; however, there is no direct experimental evidence to support it. This work attempts to build an experimental procedure to obtain experimental evidence for the proposal.

To obtain aluminium bifilms smaller than 3 mm in 12-mm diameter specimen bars, an oxide generator was designed using a gating system. Micro X-ray tomography (Skyscan 1702) was used to establish the best specimen diameter and scanning conditions, including exposure time, magnification, rotation angle and rotation-step angle. Following scanning, the specimens were re-melted for 1, 2, 3, 4 and 5 minutes at 745 °C, and then quenched in the air until solidified. They were then re-scanned to establish the changes in their defect morphologies.

In the experiments, the maximum scanning exposure time, minimum rotation step angle, maximum magnification, minimize specimen size and centring of the specimen on the specimen holder were important to obtain the best detail in the topographical results. In addition, adjusting the threshold level had an important effect on the volumetric analysis. This research could not use a re-melting method. However, in a comparison before and after re-melting processes, the surface connected defects did not change their shape. Hydrogen penetration and intermetallic effects could not be observed in this experiment. However, dendrite pushing and shrinkage could be observed.

Acknowledgements

I would like to express my deep appreciation to my supervisor, Professor Nick Green, for his mental and academic support, without which my humble work could not have been completed. I thank him for challenging me and showing me his creativity.

I sincerely thank Professor John Campbell for his great gift of encouraging me to study in Birmingham and opening my way to study castings.

I would like to thank Mr. Chris Cooper for his advice on my experiments and for helping me to use the SkyScan equipment, offering valuable time and support.

I want to acknowledge Mr. Adrian Camden and Mr. Peter Cranmer, who helped with most of my experiments. They contributed extra effort, energy and kindness to me and my work.

Finally, I could not be here without my family, who strongly supported and encouraged me. I thank them for everything.

Table of Contents

Chapter 1	- 10 -
Chapter 2	- 13 -
2.1 Aluminium Oxidation	- 13 -
2.1.1 Types of Oxides (old oxide vs. young oxide)	- 14 -
2.1.2 Entrainment Defects	- 16 -
2.1.3 Bifilms	- 19 -
2.1.4 Morphological Evolution of Bifilm Defects	- 21 -
2.1.4.1 Hydrogen Penetration	- 23 -
2.1.4.2 Dendrite Growth	- 25 -
2.1.4.3 Shrinkage	- 26 -
2.1.4.4 Intermetallics	- 26 -
2.1.5 Melt cleanliness	- 27 -
2.1.5.1 Degassing	- 27 -
2.1.5.2 Inclusion Removal	- 28 -
2.2 X-ray Imaging	- 29 -
2.2.1 3-D X-ray Tomography	- 31 -
2.2.2 Principles of X-ray Tomography	- 32 -
2.2.3 Three-dimensional Images	- 34 -
2.2.4 Spatial Resolution and Noise Control	- 35 -
2.2.5 Beam Hardening and Ring Artefacts	- 37 -
2.3 Summary	- 39 -
Chapter 3	- 41 -
3.1 Materials	- 41 -
3.2 Oxide Generation in the Mould and Specimen Preparation	- 41 -
3.2.1 Mould Design	- 41 -
3.2.2 Melting	- 42 -
3.2.3 Sand Mould	- 43 -
3.2.4 Real Time X-ray Observation of Mould Filling	- 43 -
3.2.5 Locating Oxide Defect and Specimen Preparation	- 44 -
3.3 3-D Micro X-ray Tomography Set- up	- 44 -
3.3.1 X-ray Tomography Scanning Set-up	- 44 -
3.3.2 2-D to 3-D Reconstruction Set-up	- 46 -
3.3.3 Volumetric Image Reconstruction Set-up	- 46 -
3.4 Re-melting Process of Specimens	- 47 -
3.4.1 Quartz Glass Tube with Argon	- 47 -
3.4.2 Ceramic Mould with Air Environment	- 47 -
3.5 Optical Microscopy	- 48 -
3.6 SEM and EDS	- 49 -
Chapter 4	- 50 -
4.1 Flow Behaviour and Entrainment Oxide in the Mould	- 50 -
4.2 X-Ray Film	- 51 -
4.3 Metallographic Imaging of Film X-Ray Defects	- 53 -
4.4 SEM and EDS Results for Ingot and Casting Specimens (before re-melting) and Fractured Surfaces Caused by Machining	- 56 -
4.4.1 SEM and EDS Results of Ingot	- 56 -

4.4.2	SEM and EDS Results of Casting Specimens	- 57 -
4.4.3	Fractured Test Piece Surfaces.	- 58 -
4.5	Micro-focus X-ray tomography	- 61 -
4.5.1	Relationship Between Spatial Resolution and Specimen Sizes.....	- 61 -
4.5.2	Data Acquisition Parameters with Different Exposure Times and Rotation Step Angles.....	- 62 -
4.6	Image Reconstruction Parameters.....	- 64 -
4.6.1	Hardening Correction Effects.	- 64 -
4.6.2	Ring Artefact Correction.....	- 65 -
4.7	Volumetric Images.....	- 66 -
4.7.1	Threshold Effect on Volumetric Images	- 66 -
4.7.2	3-D Images of Pores with Aluminium Oxides.....	- 68 -
4.8	Development of Re-Melting Techniques	- 70 -
4.8.1	Quartz Glass Tube with Argon Sealing.....	- 70 -
4.8.2	Ceramic Mould in an Open Environment.....	- 72 -
4.8.2.1	Re-Melting with Different Melting Times	- 72 -
4.9	Micro Tomography Scanning After Re-Melting.....	- 73 -
4.10	SEM and EDX Oxide Results in Re-Melted Specimens	- 75 -
Chapter 5		- 77 -
5.1	Technique for Developing Oxide Films Inside a Mould.....	- 77 -
5.2	Techniques for Applying X-ray Microtomography.....	- 78 -
5.2.1	Scanning Parameter	- 78 -
5.2.2	Reconstruction parameter	- 80 -
5.2.3	Volumetric Imaging.....	- 81 -
5.3	Techniques for Re-melting Bifilms in the Specimens.....	- 83 -
5.4	Bifilm Behaviours after the Re-melting Process.....	- 84 -
Chapter 6		- 88 -
Chapter 7		- 90 -
References		- 92 -

Table of Figures

<i>Figure 2.1: An SEM image of an old oxide surface [27].</i>	- 15 -
<i>Figure 2.2: A SEM image of young oxide [27].</i>	- 16 -
<i>Figure 2.3: Description of surface turbulence generation: oxide films located between liquid aluminium alloy and gas phase [6].</i>	- 17 -
<i>Figure 2.4: Balance of forces in the surface of a liquid [6].</i>	- 18 -
<i>Figure 2.5: Tangled bifilm and magnification of a portion of the bifilm [28].</i>	- 20 -
<i>Figure 2.6: The change in volume of the trapped air with the time for different alloys [7].</i>	- 21 -
<i>Figure 2.7: (a), (b), and (c) Tangled oxide layers unfurling. (d) The oxide layers follow the dendrite growing [4].</i>	- 22 -
<i>Figure 2.8 Hydrogen solubility in aluminium and two of its alloys.</i>	- 23 -
<i>Figure 2.9: Unfurling process by hydrogen penetration [4].</i>	- 24 -
<i>Figure 2.10: Schematic diagram describing the various degassing steps [48].</i>	- 28 -
<i>Figure 2.11: Schematic illustration of filter medium and cake [53].</i>	- 29 -
<i>Figure 2.12: X-ray tomography beam types: (a) cone beam, (b) fan beam and (c) synchrotron beam [56].</i>	- 31 -
<i>Figure 2.13: General principle of X-ray tomography scanning: (i) data acquisition from top right to top left of image; (ii) back projection and reconstruction from bottom left to bottom right of the image [65].</i>	- 33 -
<i>Figure 2.14: 3-D images with different voxel values: Scanned images are top row: 5 (left), 10 (centre) and 15 (right) μm voxels. Artificially degraded images are bottom row: 10 (left), 20 (centre) and 40 (right) μm voxels [71].</i>	- 35 -
<i>Figure 2.15: Field of view (FOV) for a specimen: (a)~(b) Situations where the target objects are not in the FOV, (e) right position between FOV and the specimen and (f) field of view with the interesting section [57].</i>	- 36 -
<i>Figure 2.16: Beam hardening and Ring artefacts: (a) Upper level of the picture has no hardening corrections and lower level is after hardening corrections (b) Ring artefacts [70].</i>	- 38 -
<i>Figure 3.1: Mould design for the oxide generation in the mould.</i>	- 42 -
<i>Figure 3.2: Skyscan 1702 (left)(www. Skyscan.be) and schematic of the scanning system (right) [77].</i>	- 45 -
<i>Figure 3.3: A drawing of the re-melting ceramic mould.</i>	- 48 -

<i>Figure 4.1: Real-time X-ray flow images during the filling process.</i>	- 51 -
<i>Figure 4.2: Observation of defects using a real-time X-ray machine. Defects of approximately 1 and 2.5 mm diameter are circled.</i>	- 51 -
<i>Figure 4.3: Film X-rays of 12mm diameter casting specimens before machining observed at two different orientations: 0° (left) and 90° (right).</i>	- 52 -
<i>Figure 4.4: X-ray film images from two different angles, 0° (left) and 90° (right), after machining to 8-mm diameter ((a), (b), (e) and (f)) and 5-mm diameter ((c) and (d)).</i> ...	- 53 -
<i>Figure 4.5: Metallographic sections through defects in the X-rays of Figures 4.3 and 4.4: (a) gas hole structures with oxides, (b) small gas hole structure with thin double oxide layers and (c) gas holes with thin double oxide layers that were tangled together.</i>	- 54 -
<i>Figure 4.6: Different magnifications of oxide films that were detected after polishing but not identified on the X-ray film.</i>	- 55 -
<i>Figure 4.7: Different magnifications of bifilms that were detected after polishing but not identified on the X-ray film.</i>	- 55 -
<i>Figure 4.9: SEM images ((a) and (b)) and EDS analysis ((c) and (d)) of old oxide found within ingot samples.</i>	- 56 -
<i>Figure 4.11: Shrinkage porosity of oxide layers in the casting specimens: (a) and (b) shrinkage porosity with oxide, (c) Al 100 shrinkage porosity with thin oxide layers (O₂ 5.53 wt%) and (d) shrinkage porosity with pure aluminium(%).</i>	- 58 -
<i>Figure 4.12: (a) - (d) SEM and (e) EDS images of fracture surfaces with porosity showing reduced oxygen signal.</i>	- 59 -
<i>Figure 4.13: SEM images (a) to (c) and EDS analysis (d) a surface of fractured during machining with young oxide.</i>	- 60 -
<i>Figure 4.14: 3-D images with different exposure times—(a) 2 and (b) 7 seconds with a rotation step angle of 0.90 degrees and a grey code level of 80</i>	- 62 -
<i>Figure 4.15: 3-D image obtain with an exposure time of ten seconds, a rotation step angle of 0.45° and a grey code level of 80</i>	- 63 -
<i>Figure 4.16: Volumetric reconstructed images with a binary grey code value of 130 (threshold value): (a) no hardening correction with no ring artefact correction, (b) 20% hardening correction, (c) 50% hardening correction, (d) 70% hardening correction and (e) 100% hardening correction.</i>	- 65 -
<i>Figure 4.17: Different ring artefact correction levels: images with three different sections (the lines indicate where blurring occurs) at correction levels (a) 0, (b) 5, (c) 10, (d) 15, and (e) 20.</i>	- 66 -
<i>Figure 4.18: Reconstructed X-ray microimages indicating the volumetric image area ((a)</i>	

and (c) and cross sections from 3-D images, including the volumetric selection area ((b) and (d))..... - 67 -

Figure 4.19: 3-D volumetric images before re-melting, including cross-section views: (a) 3 mm, sp1; (b) 4 mm, sp1; (c) 4 mm, sp2; (d) 4 mm, sp3; (e) 4 mm, sp4; (f) 4 mm, sp5; and (g) 5 mm, sp1; the figure beside each caption identifier denotes the maximum linear defect length. - 69 -

Figure 4.20: Reconstructed X-ray images after melting a quartz glass tube at 750 °C for 40 minutes; the arrow indicates the top of the specimen. - 71 -

Figure 4.21: SiO₂ particle inclusions, identified after re-melting inside a quartz glass tube: (a) and (b) SEM images of SiO₂ particles with oxide networks and (c) EDS result indicating SiO₂ particles. - 71 -

Figure 4.22: Re-melting 4-mm diameter test specimens at 745 °C with different holding times: (a) one minute, (b) two minutes, (c) three minutes, (d) five minutes, (e) 10 minutes, (f) 15 minutes, (g) 20 minutes and (h) 30 minutes..... - 72 -

Figure 4.23: Comparing surface connected defect position (a) before and (b) after 5minutes melting, in a 4mm diameter specimen..... - 73 -

Figure 4.24: Scanned defects, with cross-section images, after re-melting specimens with different melting times: (a) 3-mm diameter specimen for three minutes with a cross-section image, (b) 4-mm diameter specimen for 1.5 minutes, (c) 4-mm diameter specimen for three minutes, (d) 4-mm diameter specimen for five minutes and (e) 5-mm diameter specimen for five minutes..... - 74 -

Figure 4.25: Different magnification SEM images of a re-melting specimen (a)and (b); (c) represents the EDS results of O₂ (10.82 wt%), Al (76 wt%), and Si (12.54 wt%)..... - 76 -

Figure 4.26: (a) and (b) SEM images of the defect in a polished metallographic section, (c) intermetallics and (d) EDS result. - 76 -

List of Tables

<i>Table 3.1: Chemical elements of Aluminium alloy.....</i>	<i>- 41 -</i>
<i>Table 3.2: The conditions of the real time X-ray machine.....</i>	<i>- 43 -</i>
<i>Table 3.3 Optimum conditions of tomography scanning.</i>	<i>- 45 -</i>
<i>Table 4.1: Specimen diameter with spatial resolutions and magnifications of Skyscan 1702.</i>	<i>- 62 -</i>
<i>Table 4.2 Volumes of different rotation step angles and exposure times.....</i>	<i>- 63 -</i>
<i>Table 4.3 Hardening correction level and volume of the targeted defects.</i>	<i>- 65 -</i>
<i>Table 4.4 Effect of threshold level on the volume result of target object.....</i>	<i>- 68 -</i>
<i>Table 4.5 The number of defects per unit volume scanned and the volumes of targeted defects.</i>	<i>- 70 -</i>
<i>Table 4.6 Number of defects per volume in specimens and the volume of targeted oxides</i>	<i>- 75 -</i>
<i>Table 5.1 The floating velocity and drag force of targeted bifilms and the fracture force of oxide films.</i>	<i>- 85 -</i>

Chapter 1

Introduction

As part of the growing desire for and trend towards creating lightweight, high strength materials, the application of high strength aluminium alloy casting products has been increasing for decades. The automotive and aerospace industries are especially desirous of substituting lightweight aluminium castings for those of ferrous materials. However, much research is still required to fully understand the aluminium oxides and gas porosity generated during filling and solidification. To minimize gas porosity and aluminium oxide in castings, degassing and melt cleaning techniques have been developed; these techniques give the highest quality liquid aluminium condition prior to the filling process [1–3].

The problem is that the high quality liquid aluminium prepared for casting is again prone to the generation of oxides within the mould during this filling process. In the liquid condition, aluminium has a high affinity for oxygen. Oxidation occurs in milliseconds when the aluminium surface contacts atmospheric oxygen and humidity [4]. If the liquid velocity during casting is high enough (typically more than 0.5 m/s at the ingate), the liquid flow becomes surface turbulent [5]. Surface turbulence folds and entangles new oxide films. These double oxide layers contain trapped air and Campbell defines these oxide layers as bifilms [4].

Bifilms are important because the liquid aluminium and air within them react to produce further aluminium oxides and aluminium nitrides prior to and during solidification [6]. These

chemical reactions consume the gas phase, while buoyancy effects may transport the bubbles in bifilms during casting [7, 8]. Moreover, some phases can be produced on the wetted oxide side [9]. Campbell proposed that the tangled thin oxides created during the filling of the mould could become flattened or spherical in shape due to four main factors [6]:

1. Penetration of dissolved hydrogen from the liquid aluminium into the bifilm during solidification,
2. Oxides are pushed by dendrites during solidification,
3. Growth of heterogeneously nucleated intermetallic faces upon the wetted oxide side, and
4. The oxides are pulled by shrinkage.

This proposal has been argued from a theoretical standpoint. However, there is no direct experimental evidence to support these theories. To observe these furling phenomena, non-destructive scanning methods with a micrometer-scale resolution are required in order to fully resolve the bifilm morphology, along with techniques for re-melting the volume. The 3-D micro X-ray tomography technique may meet such requirements. Since the development of tomography techniques for use in medical imaging, they have been applied in various fields such as 3-D studies of paleontological specimens [10], the geosciences [11] and the paper industry [12]. In addition, 3-D tomography has been applied to the following when researching aluminium: the representation of aluminium foam, crack growth during tensile tests, semi-solid forming, grain-boundary imaging [13], cavity coalescence during superplastic deformation [14], 3-D imaging of pores and intermetallics [15] and 3-D visualization of ductile fracture [16].

The research reported in this thesis sought to introduce an X-ray tomography technique to observe the behaviour of bifilms during solidification in an aluminium casting. It first introduced aluminium oxides and X-ray tomography techniques, and then developed tomography and re-melting techniques for observations after solidification with the objective of quantifying the effect of the liquid holding time on the bifilm morphology.

This work found the best conditions for X-ray tomography techniques. However, the details of the oxide layer could not be obtained because of limited resolution. In addition, this research could not accomplish a re-melting method. However, surface connected defects did not change their shape in a comparison before and after re-melting processes. With these defects, the hydrogen penetration and intermetallic effects could not be observed through this experimental method. However, dendrite pushing and shrinkage could be observed.

Chapter 2

Literature Review

2.1 Aluminium Oxidation

Aluminium oxidation occurs when aluminium comes into contact with oxygen or humidity in the air and the reaction produces alumina (Al_2O_3). Aluminium in the liquid state reacts with oxygen within milliseconds and produces a continuous alumina layer on its surface. This oxide surface remains stable on the liquid surface because of the non-wetting behaviour between Al_2O_3 and liquid aluminium under $950\text{ }^\circ\text{C}$ [17–19]. The continuous nature of the alumina on the liquid surface prevents direct contact with air, thus retarding further oxidation.

The initial oxide layer is too thin to sustain external or internal forces. In general, alumina is thermodynamically very stable. When oxide-free liquid aluminium is exposed to air, a few tens of nanometres of thin amorphous AlO_3 (alumina) quickly cover the surface [20]. This thin oxide layer starts to crystallize from amorphous to $\gamma\text{-Al}_2\text{O}_3$ after five to ten minutes [21, 22]. Crystallization is affected by the temperature of the aluminium, the exposure time and the amorphous film thickness [21–23]. During crystallization, and the accompanying thermal expansion and volumetric contraction, tensile transformation stresses are generated within the film. Under the action of the tensile stress, local failure of the film generates surface cracks [22, 24]. The newly exposed liquid between the cracks generates new amorphous layers and these grow by the same process. After an extended period of time, a period of transformation

occurs on the liquid aluminium surface (this involves a further decrease in the volume of the oxide), whereby $\gamma\text{-Al}_2\text{O}_3$ is transformed into $\alpha\text{-Al}_2\text{O}_3$ (corundum). This reduction in volume causes further cracks, again producing new amorphous bands [22]. This continuous growth cycle continues until the films are thick enough to sustain the stresses developed at the surface. During this growth process, other forms of oxidation also occur with other chemical elements [7, 25].

2.1.1 Types of Oxides (old oxide vs. young oxide)

Campbell defined two different types of aluminium oxides, which are distinguished by their thickness. These are 'old oxide' (thick) and 'young oxide' (thin) [6]. Old oxides develop from the thickening of the oxide that originally exists on the surface of ingots during the melting process and also during the transport of the liquid from a furnace to a crucible. As their name implies, old oxides form under longer exposure times to an oxidizing atmosphere; so they have time to grow thick. Such thick oxide films are often semi-rigid and thus less prone to deformation under the action of free surface turbulence during the filling process. As a result, they have fewer and coarser deformation wrinkles than a young oxide film observed at high magnification using a scanning electron microscope (Figure 2.1) [26].

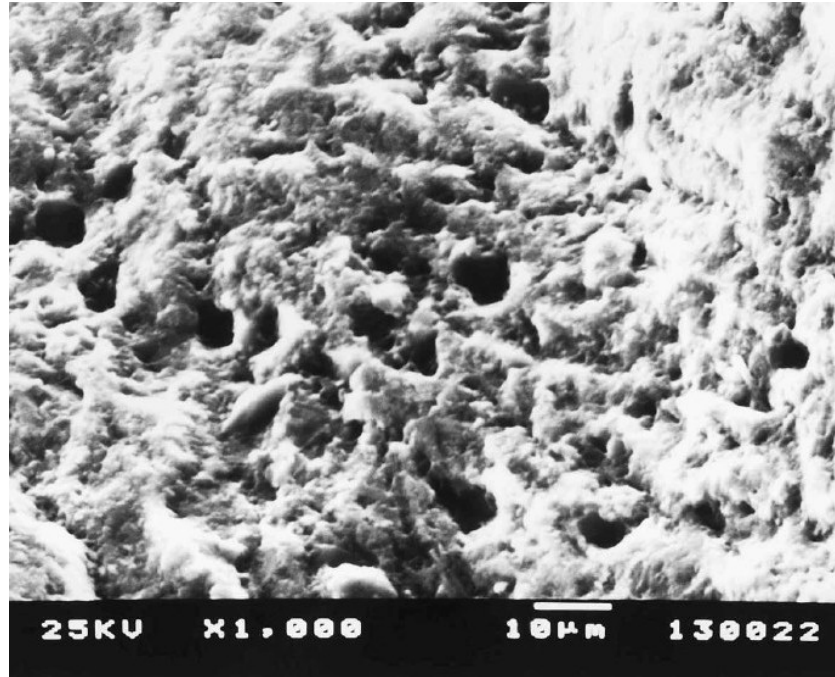


Figure 2.1: An SEM image of an old oxide surface [27].

The extremely rapid reaction of liquid aluminium with air can produce aluminium oxide during the filling process [4]. During mould filling, the liquid metal free surface can be unstable or expanding, exposing fresh liquid aluminium to air and humidity in the mould, producing thin aluminium oxides called ‘young oxide’. However, unlike old oxide, young oxide has an extremely short exposure time to air. Hence, young oxides are reported to be amorphous Al_2O_3 with thicknesses of only a few nanometres [20]. These thin oxide layers fold easily and may become tangled by the internal bulk flow turbulence once incorporated into the liquid and remain as complex double oxide layers in the casting. The general shape of a young oxide has many thin sharp edges (wrinkles), as shown in Figure 2.2. If held in the liquid alloy, some of these oxides may bond or grow into each other. However, the majority of young oxides trap air between their films [28]. These oxide layers containing air are defined as bifilms. A detailed explanation of the formation and characteristics of bifilm defects is given in the following sections.

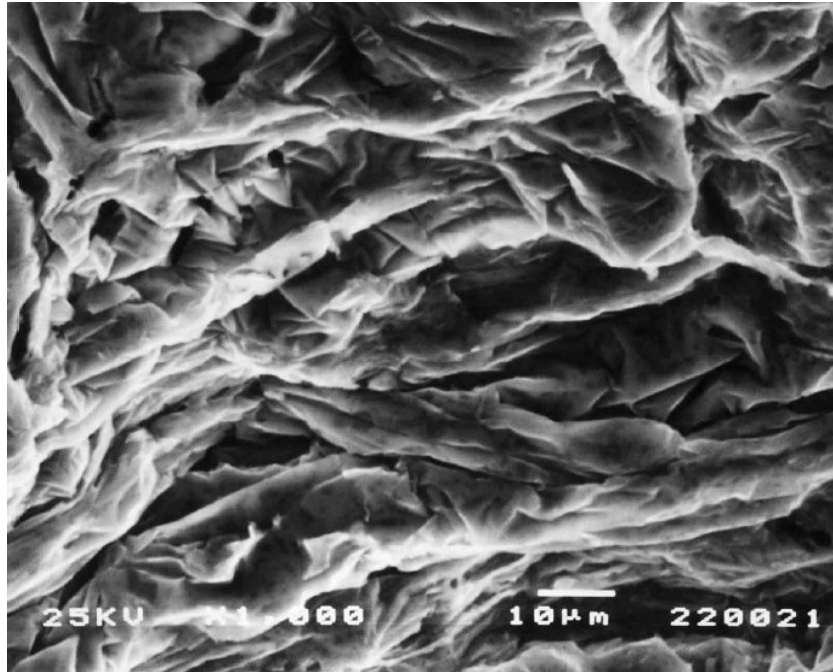


Figure 2.2: A SEM image of young oxide [27].

2.1.2 Entrainment Defects

When in the liquid condition, aluminium and aluminium alloys are extremely reactive with oxygen. Therefore, aluminium oxidises readily during the melting and filling processes. This is often compounded by an increase in the surface area of the aluminium liquid during flow. The first possible source of oxides in castings is the ingot metal itself, not only on the aluminium ingot surface but also in the aluminium as internal defects. These aluminium oxides remain stable in the molten aluminium. In addition, heating methods facilitate the growth of oxides and air convection may bring inclusions such as ceramic particles from furnace linings and large dust particles onto the surface of the aluminium [6]. If these inclusions are heavy enough, they break through the oxide into the melt. These inclusions attach to the oxide layers and may become incorporated into the melt as part of a bifilm defect [6].

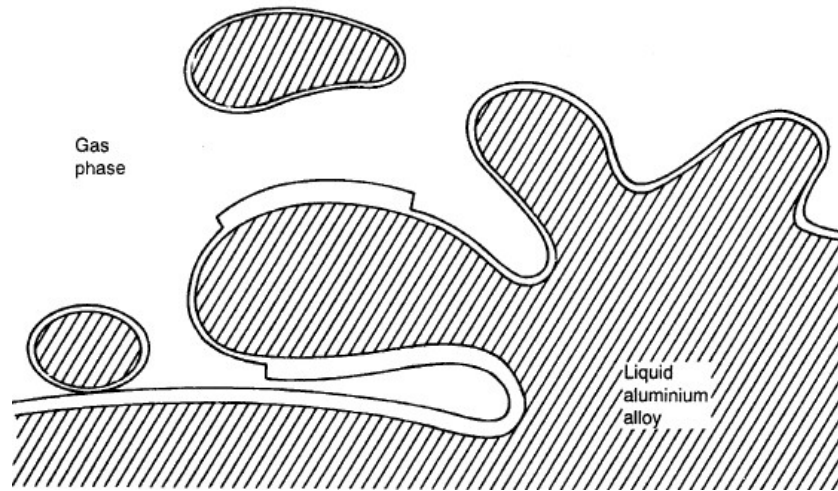


Figure 2.3: Description of surface turbulence generation: oxide films located between liquid aluminium alloy and gas phase [6].

The amount of oxide entrained in the liquid metal during the filling portion of a casting process depends on the degree of free surface turbulence that occurs. Free surface turbulence can be considered to be the uncontrolled folding of the liquid metal surface onto itself or, in more severe cases, the formation of metal drops by the disintegration of the liquid surface (Figure 2.3).

Campbell defined ‘surface turbulence’ using a dimensionless flow quantity called the Weber number, We [6]. The Weber number is the dimensionless ratio between the internal pressure exerted upon the melt surface ($\rho V^2/2$) and the surface tension ($2\gamma/r$) of a hemispherical deformation. Thus:

$$We = \rho L V^2 / \gamma$$

where ρ : density of the liquid, V : velocity of the liquid, L : flow length, which can be expressed as r (radius of the hemisphere) and γ : the surface tension of the liquid.

If the internal pressure acting upon the surface is less than that arising due to surface tension, then $We < 1$ and no surface turbulence occurs [6]. However, when the internal pressure is

equal to ($We = 1$) or higher ($We > 1$) than the surface tension forces, surface turbulence will occur. As the We value increases, the severity of the turbulence increases.

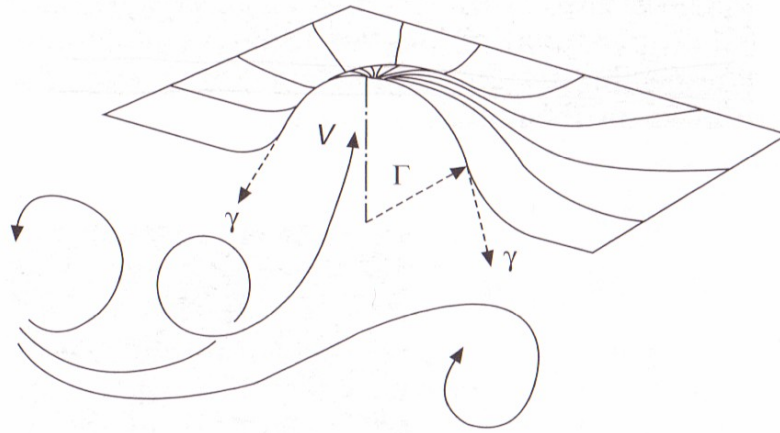


Figure 2.4: Balance of forces in the surface of a liquid [6].

When the internal pressure is equal to the surface tension, the velocity at this condition can be the critical velocity of surface turbulence [6]. Therefore, $\rho V^2/2 = 2\gamma/r$ (Figure 2.4), such that

$$V_{\text{crit}} = 2(\gamma/r\rho)^{1/2}.$$

Assuming ‘ r ’ to be half the sessile drop height, Campbell calculated the critical velocity of liquid aluminium at an ingate to be close to 0.5 ms^{-1} . Runyoro and Campbell designed an experiment to determine the critical ingate velocity of aluminium alloys, and proved that the critical gate velocity for the generation of surface turbulence was 0.5 ms^{-1} [29]. At velocities greater than 0.5 ms^{-1} at the ingate, the turbulence increased the liquid aluminium surface contact area with air and generated several types of oxidized surfaces such as a single surface oxide layer and multiple entrained oxide layers that were tangled [30].

Aluminium oxide bifilms can also be produced as a result of the geometry of the mould. During mould filling, some geometries may cause the aluminium to fall to lower levels.

Falling leads to the formation of a tube of oxide around the liquid surface and this exists as the lower level of the mould is filled. Periodically, this oxide tube may detach from the stream, falling with it and becoming incorporated (entrained) within the liquid pool, which is a consequence of the plunging metal jet [6]. During filling, such fluid falls also generate surface turbulence and produce other aluminium oxides.

Air bubbles formed during filling also generate aluminium oxide on their surfaces. Air bubbles are highly buoyant and float to the coasting surface. Campbell described how the motion of entrained bubbles can lead to the formation of oxide strings, a defect for which he coined the term bubble trails.

2.1.3 Bifilms

As described previously, the surface turbulence entrains folds and causes tangled networks of thin aluminium oxides when filling a mould. These folded or tangled oxides consist of double oxide layers with air in between. Because of the high sintering temperature of alumina, they are un-bonded and act as cracks within the liquid that are frozen into the solid. Moreover, the un-wetted rough surface oxides, particularly ‘old oxide’, cannot fold together perfectly and an air gap remains between the rough surface layers. Examples of layers of aluminium oxide defects (called ‘bifilm’) are shown in Figure 2.5 [31].

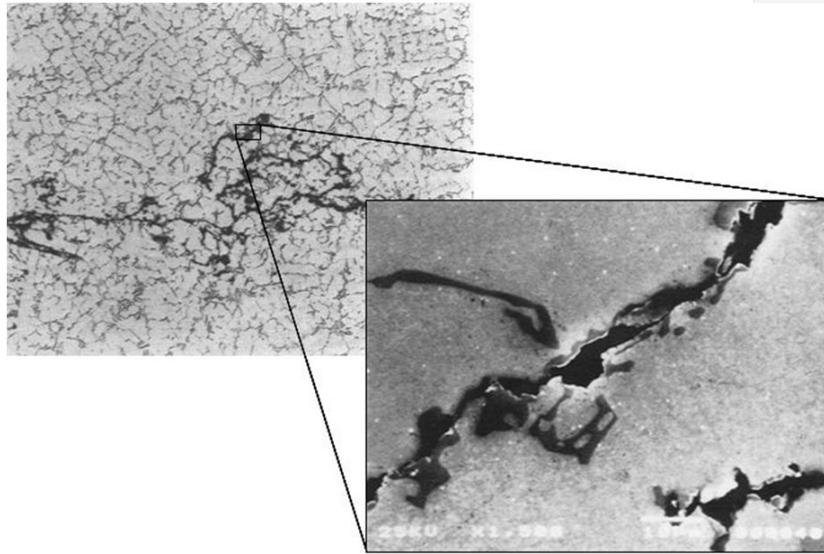


Figure 2.5: Tangled bifilm and magnification of a portion of the bifilm [28].

Due to the imperfect joining of the oxide films, a layer of air is trapped between them. The air inside the bifilm continues to react with gases such as oxygen and nitrogen to form Al_2O_3 and AlN , causing the internal gas pressure to fall and bringing the films together [32]. Opposing the collapse of the film through oxidation is the precipitation of hydrogen in the liquid, which may make the bifilm expand [4]. Thus, it can be inferred that once formed, the nature or characteristics of bifilm defects may continue to change or evolve while in the melt. Compounding this may be the fact that the trapped gas confers buoyancy to the defects. However, at the same time, the films may sink because the oxidation reaction consumes the atmosphere [33]. Such expansion and contraction remain poorly understood and cannot be modelled with great accuracy; thus, the positions of bifilms are hard to predict in a casting.

Raiszadeh and Griffiths observed the progressive reaction of air bubbles in liquid aluminium [7]. They held a large air bubble in pure liquid aluminium and monitored its behaviour over time. As a result, they showed the first reaction with oxygen to form alumina. After the supply of oxygen was exhausted, the aluminium reacted with nitrogen and produced

aluminium nitride. As these reactions proceeded, the volume of the air bubble was reduced [7]. This effect is shown in Figure 2.6.

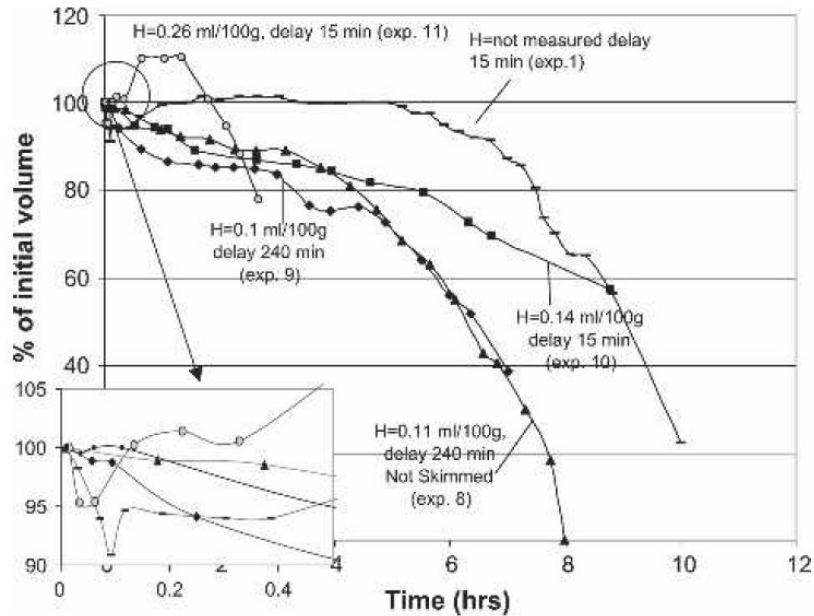


Figure 2.6: The change in volume of the trapped air with the time for different alloys [7].

2.1.4 Morphological Evolution of Bifilm Defects

The high filling velocity that often arises during the casting of aluminium generates surface and internal turbulence in the mould. While surface turbulence will entrain the aluminium oxide film, the forces acting in various directions upon the film, which possesses negligible strength, may cause it to be folded, tangled and sometimes broken into small pieces by internal turbulent forces [4]. One effect on the bifilm shape can be to change it from the long and wide oxide surface associated with surface folding into a small round shape that is highly tangled (e.g. Figure 2.5). Campbell called this process ‘furling’ [6].

Campbell also proposed a complementary ‘unfurling’ process that starts during solidification with contributions from four main factors: hydrogen penetration, dendrite growth, shrinkage volumetric contraction and intermetallic growth (Figure 2.7). Dissolved hydrogen penetrates inside the tangled bifilm and fills the gap between the two oxide layers. This hydrogen pressure pushes apart the surfaces of the oxide layers, inflating them and making them spherical in shape. The growing dendrites push the tangled surfaces straight. In addition, shrinkage opens up the two oxide layers and the intermetallics generate surface tension forces on the wetted oxide surface, potentially contributing to un-furling.

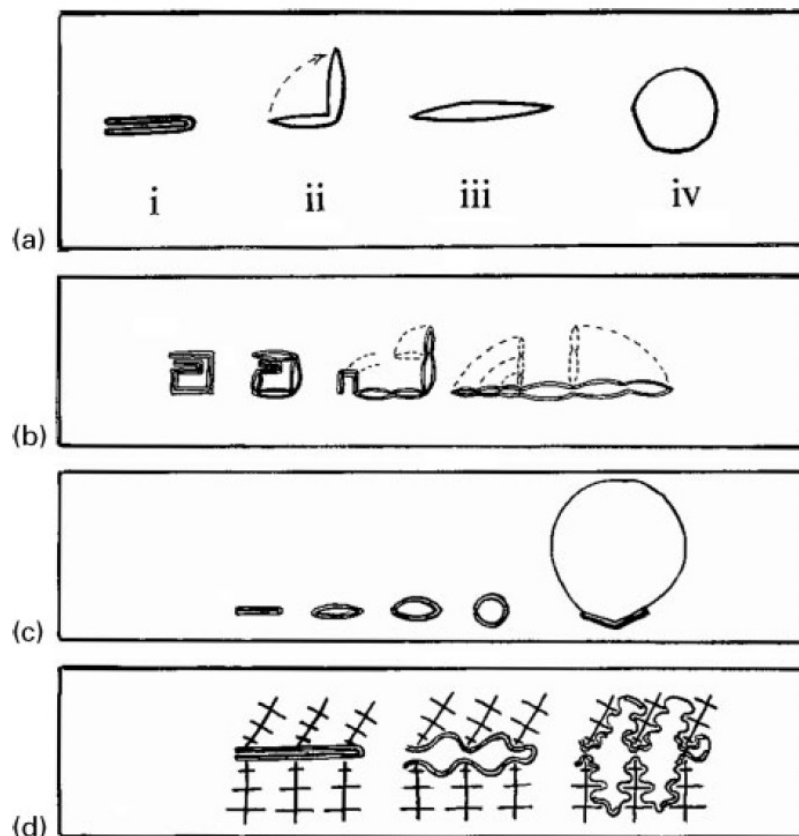


Figure 2.7: (a), (b), and (c) Tangled oxide layers unfurling. (d) The oxide layers follow the dendrite growing [4]

2.1.4.1 Hydrogen Penetration

The hydrogen solubility in liquid aluminium is ten times higher than in solid aluminium, and the solubility increases when the temperature increases (Figure 2.8) [34–36]. On cooling, the solubility falls and the dissolved soluble hydrogen in the liquid aluminium achieves a supersaturated condition and starts to dissolve as the temperature decreases during solidification. This dissolved hydrogen penetrates into the interdendrite or granular liquid and forms pores at grain boundaries or dendrite cell gaps [34, 37].

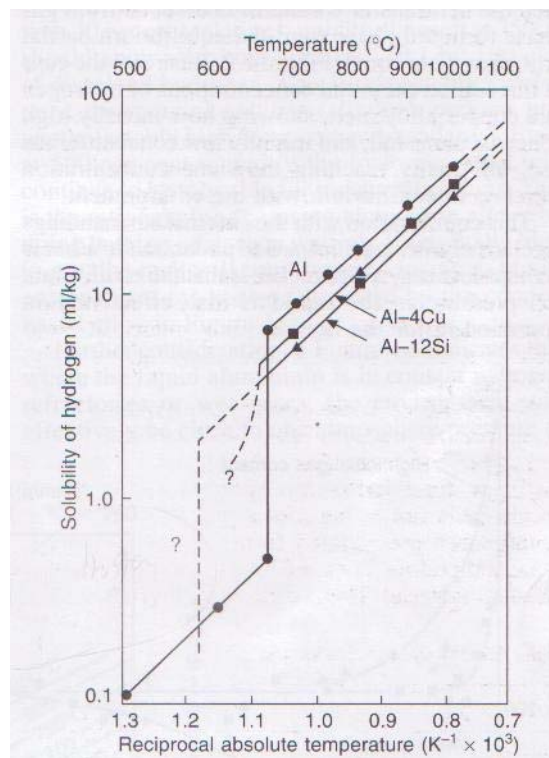


Figure 2.8 Hydrogen solubility in aluminium and two of its alloys.

Hydrogen penetration also occurs in bifilms during solidification. Campbell described the unfurling model mechanism driven by hydrogen dissolved in the liquid (Figure 2.9). He assumed that if the unfurling force is related to the viscosity of the liquid aluminium, then the

unfurling occurs when the pressure inside the bifilm is the same or higher than the viscous drag force resisting the motion [4]. Using Stokes's law, the force resisting unfurling ($3\pi\eta RV/2$) can be equated to the hydrogen penetration pressure ($2PRh(h/2)$) (Figure 2.9), where P : hydrogen penetration pressure, η : viscosity of the liquid, R and h : width and height of the pressure unfurling the bifilm?

When the resistance force is the same as the hydrogen penetration pressure, the oxide starts unfurling. Thus, when the forces acting on the average height (half of the height),

$$2PRh(h/2) = 3\pi\eta RV(R/2)$$

for the duration of unfurling (t), the velocity V can be substituted by $\pi R/t$:

$$t = (3\pi^2/2)(\eta/P)(R/h)^2.$$

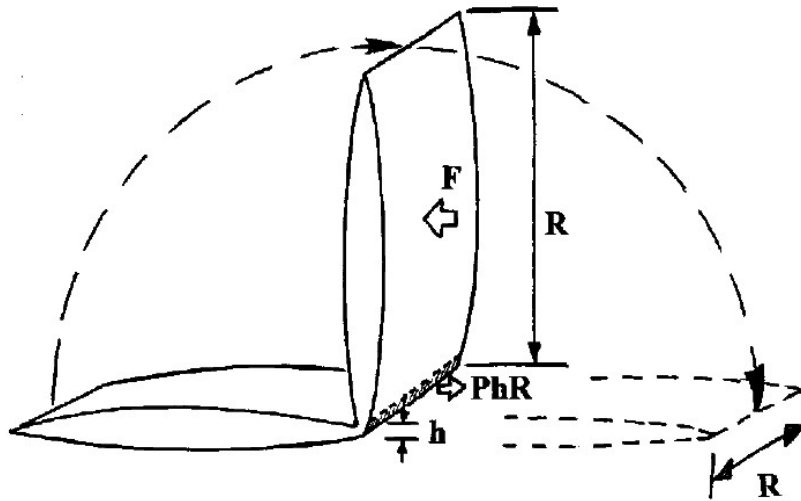


Figure 2.9: Unfurling process by hydrogen penetration [4].

The solubility of hydrogen in liquid aluminium can be changed primarily by the melting conditions, melt treatment or alloying and modification elements. During the process of melting the aluminium, the liquid aluminium contacts and reacts with the humidity that is present in or on the furnace, charge materials, fluxes and furnace tools. Hydrogen gas can

dissolve during this chemical reaction between aluminium and humidity as $4/3\text{Al} + 2\text{H}_2\text{O} \rightarrow 2/3\text{Al}_2\text{O}_3 + 4\text{H}$. Using a heating fuel that contains hydrocarbons can also increase the hydrogen content of aluminium melts. Increasing the temperature and holding time can increase the dissolved hydrogen content [38]. The solubility of the hydrogen will increase as the temperature increases; the degassing time required to remove hydrogen from solution doubles as the temperature increases by 60 °C [39].

The alloying and modification of aluminium alloys also affects the solubility of hydrogen. Cu, Si, Zn and Fe can reduce the solubility of hydrogen, and Mg, Li and Ti can increase the hydrogen solubility [35]. The effect of strontium on hydrogen solubility is still being researched [40].

2.1.4.2 Dendrite Growth

During the solidification of aluminium alloys, the primary α -Al phase grows with a dendritic structure [41]. When the growing dendrites impinge upon a bifilm, they cannot grow through the film and their advance is arrested [4, 31]. According to Campbell, these primary and secondary dendrites push against the oxide surface during solidification [4]. The pushed, furled oxide turns into untangled or flattened oxide as it is pushed between dendrite boundaries. It was suggested by Campbell that the many oxide layers observed at grain boundaries prove this phenomenon (see Figure 2.7(d)) [6]. However, there is no direct evidence to support this model.

2.1.4.3 Shrinkage

As aluminium and aluminium alloys solidify, they undergo a volumetric contraction. Often, a casting freezes from the outer surface to the interior. Feeding is used to overcome this contraction in cases where there is a local deficit of feed metal. According to Campbell [4], the force that is generated by the negative pressure arising in the liquid aluminium at the solidification area acts on the entire surface area of a bifilm and separates the area of the two oxide layers [6]. The shrinkage effectively drapes oxide films over the dendrite surface (Figure 2.7(d)). Shrinkage forces may well assist a tangled oxide to unfurl.

2.1.4.4 Intermetallics

Inclusions come into the melt in various ways such as ceramic particles or sand from the furnace, dust from the equipment and chemical reactions during the melting and holding processes. Inclusions from the melting process can be effectively removed by the degassing process and the use of filters in the mould [42]. Intermetallics are sometimes observed on the wetted side of the oxide. Entrained aluminium oxide in liquid aluminium is comprised of a dry surface contacting gas and a wetted surface contacting the aluminium liquid. The non-wetted surface reacts with the air inside the bifilms and produces oxide layers [7, 8]. Cao and Campbell observed Fe-types of intermetallics, such as $\text{Al}_{15}(\text{FeMn})_3\text{Si}$ or $\text{Al}_{15}(\text{FeMnCr})_3\text{Si}_2$ on the wetted surface [43, 44].

It has been suggested that the brittle intermetallics formed on a wetted oxide surface help with the unfurling of bifilms. According to Campbell, growing intermetallics, especially the

β -Fe plate, unfurl the tangled bifilm [6]. Initially, the intermetallics on an oxide surface are thin enough to bend; however, their stiffness increases as their thickness grows. The intermetallics try to have a flat shape, with their growth generating sufficient force to deform and straighten the shape of the oxide.

2.1.5 Melt cleanliness

2.1.5.1 Degassing

The amount of hydrogen dissolved in the liquid aluminium can often define the amount and size of the porosity defects [45]. To remove hydrogen from the liquid aluminium, a degassing process is essential. Flux, purge gasses, vacuum degassing and ultrasonic vibration can be used as degassing methods [3]. The most popular method is bubbling inert or reactive gases from near the bottom of the furnace. The purge gasses are usually Cl_2 , SF_6 , Ar or some mixture of these gases. During their passage through the melt, the bubbles, which are of low initial hydrogen content, absorb hydrogen from the melt and then escape at the surface. The melting temperature, size of the gas bubbles and gas composition are important factors for this degassing method [39, 46]. The solubility of hydrogen doubles when the liquid aluminium temperature increases by $60\text{ }^\circ\text{C}$ [1]. The size of the gas bubbles determines the area/volume ratio (A/V). For high degassing efficiency, the A/V should be maximised, and bubble smaller than 5 mm are the most effective [46]. According to many researchers, rotary impeller degassers (Figure 2.10) can produce metal virtually free of dissolved hydrogen [39, 42, 47]. In addition, this method of degassing can remove solid inclusions from the melt by flotation when bubbles attach to them.

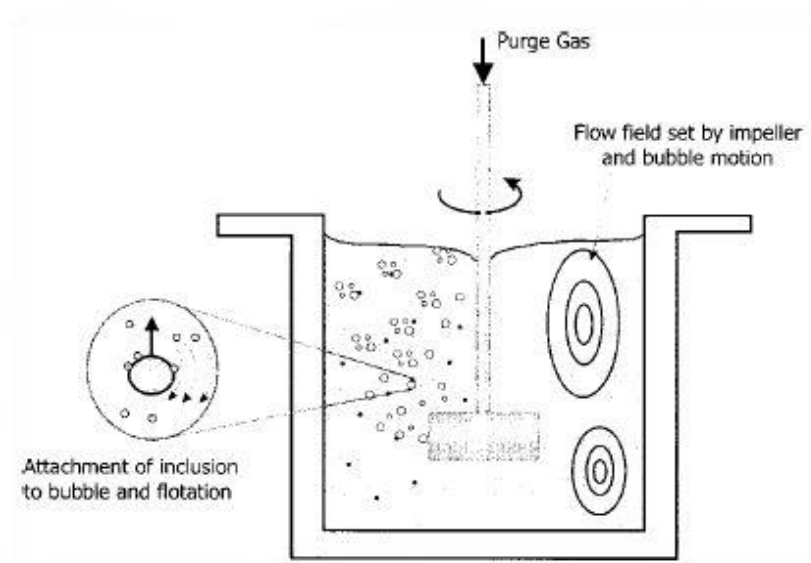


Figure 2.10: Schematic diagram describing the various degassing steps [48].

2.1.5.2 Inclusion Removal

Inclusions such as aluminium oxide and $MgAl_2O_4$ (spinel) come from ingots or reactions with oxygen in the air or humidity during melting and casting. Other inclusions are formed by chemical reactions with alloy elements in the melt. Sedimentation, flotation and filtration in the furnace are used by the foundry industries to remove these inclusions [3].

Aluminium oxides and magnesium oxides usually exhibit slow settling (no gas contained between the oxides) or floating gas contained between oxides in the aluminium melt because of their lesser or greater densities compared with the liquid aluminium. Buoyant low density fluxes help bring such inclusions to the surface [2, 3]. Once at the surface, they can be removed by skimming. However, these fluxes contain harmful elements such as Cl, F or P. In addition, the humidity contained within the fluxes can actually add hydrogen to the melt. The flux itself can be an inclusion in the casting if it remains in the melt after treatment.

After cleaning during the melting process, a filter within the mould can help to remove inclusions such as fluxes, ceramic particles or oxide film during the filling process [3, 47]. Inclusions can be trapped on the front or entry face of the filter, and build up filter cake layers (Figure 2.11). These filter cake layers also act like filters [49, 50]. The filter types include fibreglass cloth, steel gauze screen, wire wool and ceramic foam filters [3]. The most effective of these is the ceramic foam filter because its three-dimensional network of pores provides a non-linear flow path for filtering and smoothing the metal flow [51, 52]. The cloth and screen types have a linear flow path, which has limited filtration ability, and may, in fact, generate surface turbulence, entraining air [50].

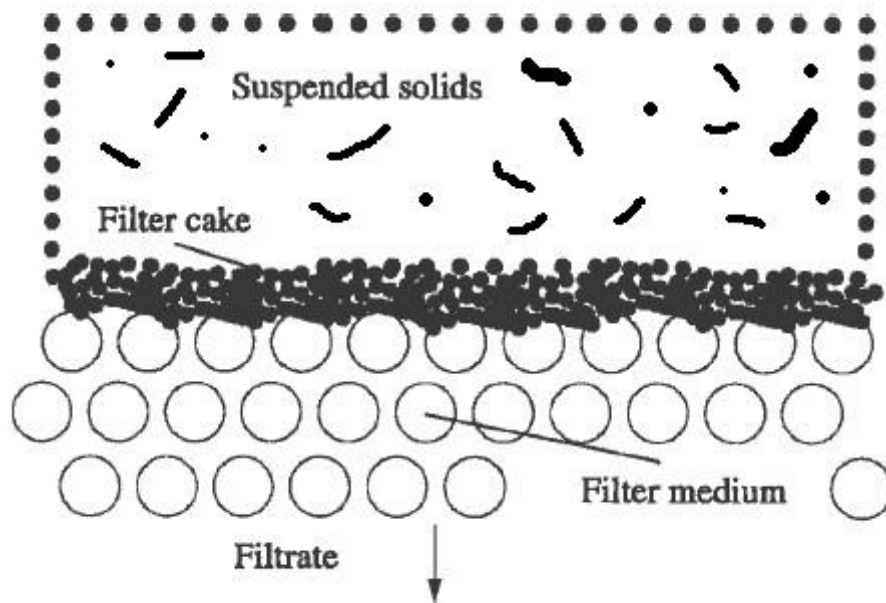


Figure 2.11: Schematic illustration of filter medium and cake [53].

2.2 X-ray Imaging

Since the development of X-ray techniques, these have been used, not only in the medical

field, but also in various sciences and engineering fields as a non-destructive inspection method. In the aluminium casting field, radiography has been an essential method to observe gas porosity and shrinkage inside castings. The development of real time radiography from the film technique has made examination faster, and the method now allows the observation of the inside of a mould during the pouring process in real time [54]. This has the potential to reduce the cost and time needed to develop industrial filling systems. In addition, Micro X-ray tomography methods make it feasible to observe micro-defects and their behaviours.

X-ray signals are electromagnetic waves with shorter wavelengths than visible light. X-rays can be defined by their wavelengths, which lie in the range of 30×10^{15} Hz to 30×10^{18} Hz. X-rays are generated by high voltage electrons inside a high vacuum tube containing electrodes (cathode and anode). When high energy electrons impact and interact with a target, X-rays are generated.

X-rays can be separated into continuous and characteristic. Continuous X-rays are also called 'white radiation' or 'Bremsstrahlung'. Electrons are scattered in the strong electric field near the nuclei of a material. When the incident electrons are decelerated by displacing electrons from the inner shell of a metal atom (X-ray fluorescence), continuous X-rays are generated.

The characteristic X-ray spectrum (fluorescence) is not like the Bremsstrahlung. Instead, when an electron in the K-shell is bombarded by an incident electron beam, it is able to obtain enough energy to overcome the attraction of the nucleus. The amount of energy required to escape from the nucleus is called the 'binding energy of the K-shell' or 'absorption energy' [55]. This energy value is dependant on the characteristics of the material

and increases with the atomic number of the element. If one of the K-shell electrons obtains this absorption energy, the electron is displaced, leaving an empty space in the K-shell. This empty space is filled by an electron from one of the higher energy shells. During this filling from the high energy level to low energy level, the replaced electron needs to emit energy. The amount of emitted energy is the difference between the high energy level of the shell donating the replacement electron and the low energy level of the shell with the vacancy. Each material element has its own energy values. Hence, the X-ray wavelength depends on the energy difference between two shells, which depends on the material.

2.2.1 3-D X-ray Tomography

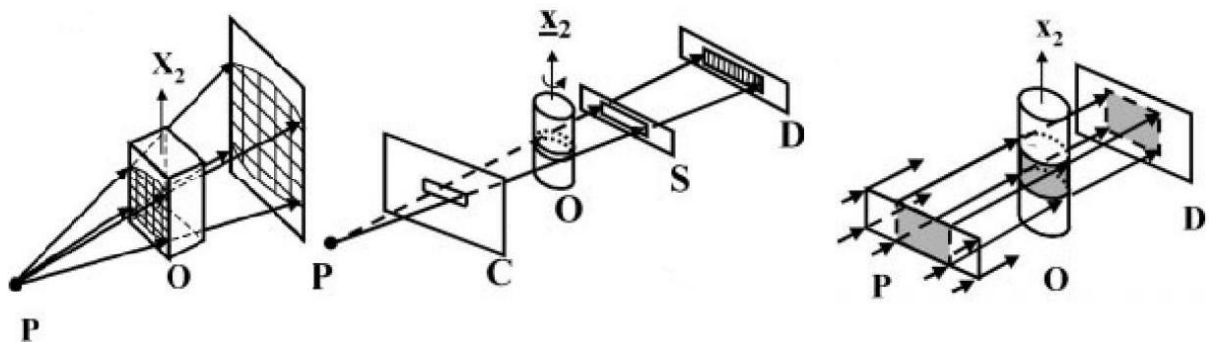


Figure 2.12: X-ray tomography beam types: (a) cone beam, (b) fan beam and (c) synchrotron beam [56].

The X-ray tomography technique was first developed in the 1970s by Hounsfield using a computed tomography system for medical imaging [56]. This technique has since been refined with more powerful and higher resolutions and shorter scanning times. Recently, commercial high performance equipment has been developed that can reach a spatial resolution of 1 μm with cone or fan beam algorithms (Figure 2.12) [56, 57]. In addition,

research equipment in The European Synchrotron Radiation Facility (ESRF) in Grenoble, France can reach a spatial resolution of 0.7 μm as a beam resolution. However, this facility can achieve voxels of up to 0.3 μm (a voxel is defined in Section 2.2.3) using their 0.7- μm resolution beam with a magnification technique [58]. These high performance scanning developments can be applied to various research fields such as archaeology, water, soil science and the timber industries [59]. In particular, this non-destructive means of determining a wide range of properties, along with the extremely high sensitivity of the X-ray tomography technique, can be used to identify the characteristics of a metal by observing phase contrast, intermetallics, porosity shape and the growth of cracks in aluminium and its alloys [58, 60–64].

2.2.2 Principles of X-ray Tomography

The principle of X-ray tomography scanning is that X-ray information about multiple one-dimensional layers is acquired from a linear array detector and used to reconstruct a two-dimensional image; multiple two-dimensional images are then used to reconstruct a three-dimensional image. A thin vertical X-ray beam passes through an object in the field of view, X-rays are absorbed by the object and the transmission intensity decreases (Figure 2.13(i)). A scintillation detector converts the transmitted X-rays into visible light. This visible light is converted into digital data using a visible light charge coupled device (CCD) camera. Multiple linear slices are obtained by rotating the specimen about the vertical axis through a series of equal increment steps (around 0.9° or less per step) until the sample has rotated through 180 or 360 degrees (Figure 2.13(ii)). The scanned one-dimensional information is called a ‘shadow image’. To accurately locate a position within the object, shadow images

with different angles of view are required. The intensity differences between the shadow images in the memory are analyzed by a computer intensive reconstruction algorithm, generating a series of two-dimensional images [66]. Each two-dimensional image is stored on a device such as a hard drive. This scanning process is called ‘back projection’. Decreasing the rotation step angle (which is the same as increasing the number of back projections) can give a sharper image (Figure 2.13(ii)) [57].

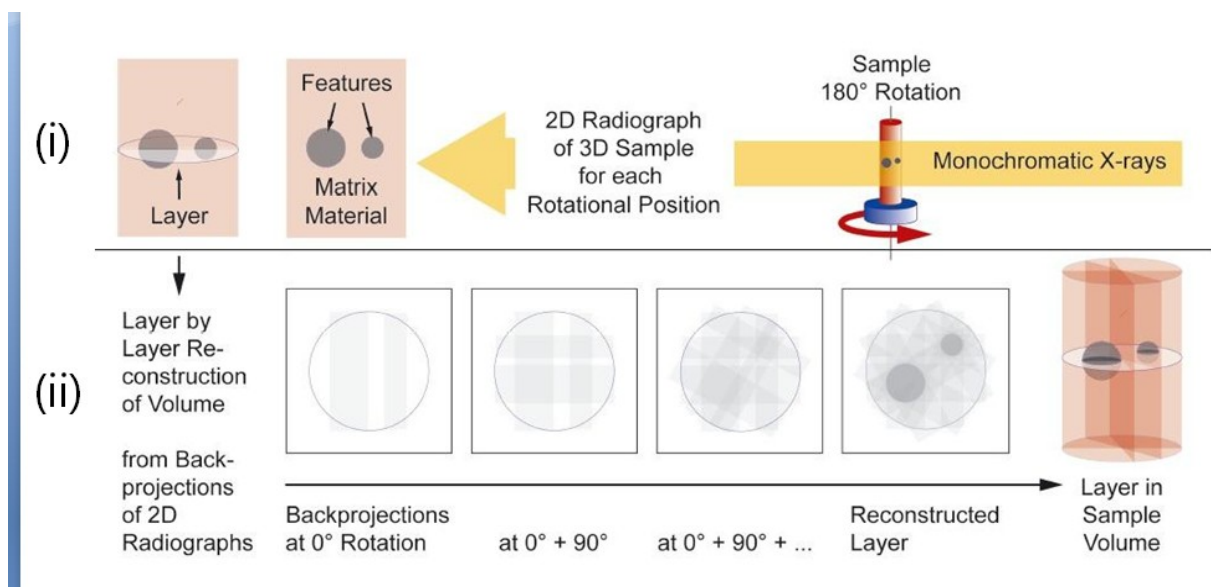


Figure 2.13: General principle of X-ray tomography scanning: (i) data acquisition from top right to top left of image; (ii) back projection and reconstruction from bottom left to bottom right of the image [65].

Once the scan is complete, the two dimensional images are reconstructed using reconstruction software and a cone beam or fan beam filtered back projection algorithm and converted into a three-dimensional image [67]. These reconstructed images are saved as cross-section images. This three-dimensional information can be converted into volumetric three-dimensional images consisting of voxels using the volume graphics software. Detailed

information about volume graphic images will be discussed in the next section.

2.2.3 Three-dimensional Images

N-dimensional digital images consist of spatial elements called 'pixels' in two-dimensional images and 'voxels' in three-dimensional images. Each spatial element has a numerical code called a grey code, consisting of integers ranging from 0 to 255 (black = 0 to white = 255) [68]. In general, gray and coloured images are based on this grey code. From these grey and coloured images, one can easily distinguish the edges or sharp objects. However, to avoid the intermediate shades of grey that may occur, grey values of the set [0,1] are used for accurate image analysis [69]. This grey code uses 0 (switch on = white) and 1 (switch off = black) and is called the binary image. The black voxels indicate that the object is considered in the foreground of the image, whereas white voxels act as the background of an image. The computer indicates '0' and '1' as background and objects from binary images. Three-dimensional images are built up using stacks of these binary images. For the observation of void defects in materials, the options of '0' and '1' needed to be changed to 0 = object and 1 = background (note: some programs have an 'inverse' option).

The grey code threshold that is used to binarise data generates a 3-D volumetric image. The use of a low level of grey code can reduce the noise in a 3-D structure; however, it can also generate holes in the surface of the structure or reduce the volume from the original volume [69]. A high level of grey code can add more volume to the structure, but at the expense of more noise from unwanted signals.

2.2.4 Spatial Resolution and Noise Control

Collecting only a limited number of X-rays with the X-ray detector generates unwanted uncertainty in the image signals, called noise. This noise is strongly related to the spatial resolution and exposure time [70]. In addition, noise can be affected by specimen geometry and size, rotation step angle and possibly magnification [56, 57].

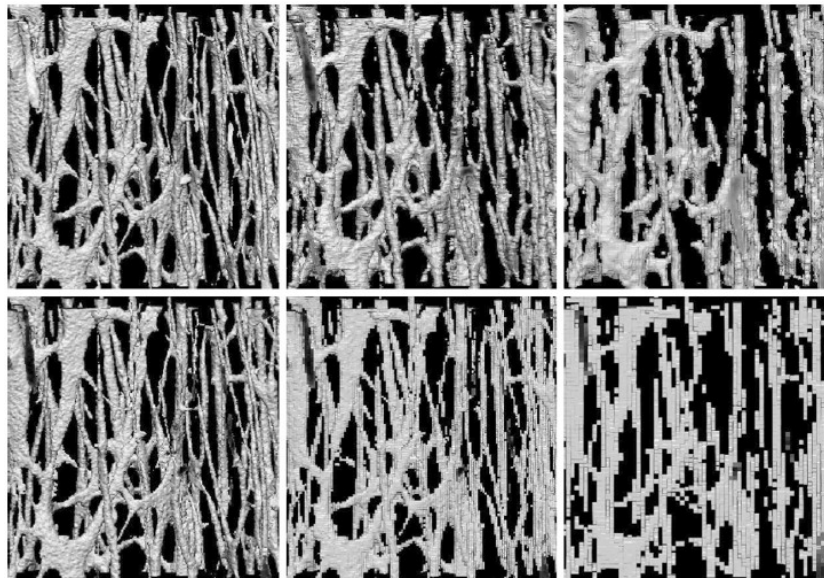


Figure 2.14: 3-D images with different voxel values: Scanned images are top row: 5 (left), 10 (centre) and 15 (right) μm voxels. Artificially degraded images are bottom row: 10 (left), 20 (centre) and 40 (right) μm voxels [71].

The spatial resolution affects detail discrimination and the quantitative analysis of volumetric 3-D images. Therefore, achieving the smallest possible spatial resolution is an important factor for X-ray tomography scanning (Figure 2.14) [71]. The spatial resolution unit for volumetric image analysis is called a ‘voxel’. The voxel size (Vox) is related to the field of view (FOV) of the detector and the number of X-ray elements that the detector can detect. The equation for this relationship is $\text{VOX} = \text{FOV} / \text{number of detections}$. The field of view is

the width and height of the scanning area. The specimen needs to be centred and inside of the FOV. If the specimen is not inside the FOV or centred in the rotator of the specimen holder, some part of the specimen will be in and another out of the scanning area, which can cause mismatched signals during the rotation (Figure 2.15) [57]. Furthermore, if the specimen is not on the centre of the FOV, specimen wobble and rotation axis misalignment can be generated during the reconstruction. Hence, it is important to locate the specimen inside the FOV in the centre of the specimen holder to get accurate results with less noise.

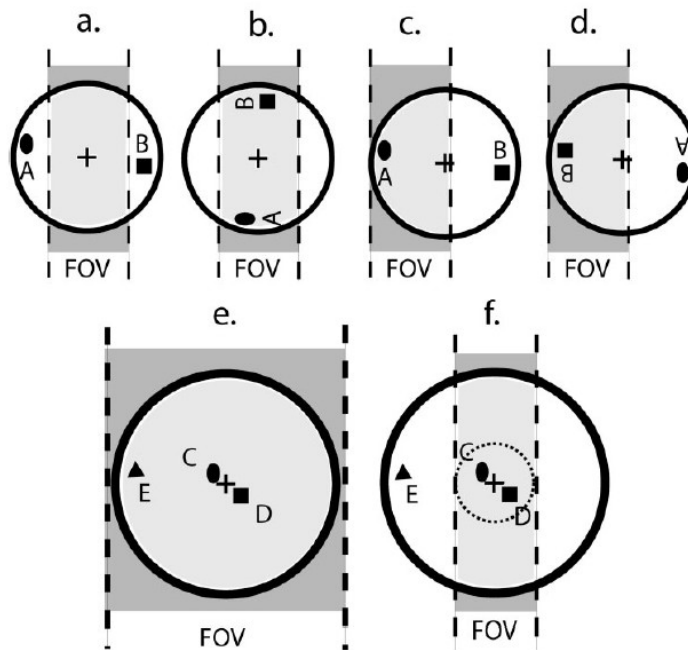


Figure 2.15: Field of view (FOV) for a specimen: (a)~(b) Situations where the target objects are not in the FOV, (e) right position between FOV and the specimen and (f) field of view with the interesting section [57].

The specimen geometry is also an important factor for spatial resolution and noise reduction. A cylindrical specimen geometry with a minimum specimen size can help improve the resolution of the scan. Since the scanning field is a cylinder pattern, a symmetrical shape for a specimen can reduce the noise during rotational scanning [11]. In addition, if a specimen has edges, these generate worse streaking during angular scanning [57]. Minimizing the specimen

size can help to improve the resolution [71]. A small specimen can result in a stronger signal during the scan, thereby reducing the noise signal.

Increasing the exposure scanning time and reducing the specimen rotation angle can reduce the noise signals [72]. When the X-ray beam passes through the target specimen, the total number of X-rays that comprise the image depends on the exposure time. When the exposure time increases, the noise signal decreases. The exposure time can increase the contrast level because of the amount of X-rays received. Furthermore, decreasing the specimen rotation angle produces more detailed information about the inside of a specimen, making the image sharper and more accurately positioned [57]. If the rotation angle is decreased to half the size of the original angle, the scanning information and scanning time will double.

Magnification is also a good method to improve spatial resolution. The concept of magnification is related to the distance between the specimen and the X-ray source. Cone and fan beams come from a single point source (P in Figures 2.12(a) and (b)) toward the detector area (D in Figures 2.12(a) and (b)). When the specimen is close to the point source, the scanning area will be smaller, but the scanning magnification will increase. Therefore, greater magnification occurs when a specimen is moved towards the X-ray source. When the specimen moves towards the X-ray source, the spatial resolution decreases with a decrease in the cone angle.

2.2.5 Beam Hardening and Ring Artefacts

Beam hardening is the most common artefact in X-ray tomography scanning. Hardening

means that the energy absorption rate of lower energy photons is higher for the target object than higher energy photons. The lower energy absorption increases when the beam passes through a specimen. When the X-ray beam passes through the specimen, the centre of the specimen observes lower energy than the edge of the specimen. Thus, the beam hardening occurs at the centre of the specimen. This hardening effect makes the specimen appear to be less dense in the centre [70]. Beam hardening can be reduced using an attenuation filter, a smaller sample and correction during image reconstruction [73]. An illustration of beam hardening and ring artefacts is shown in Figure 2.16.

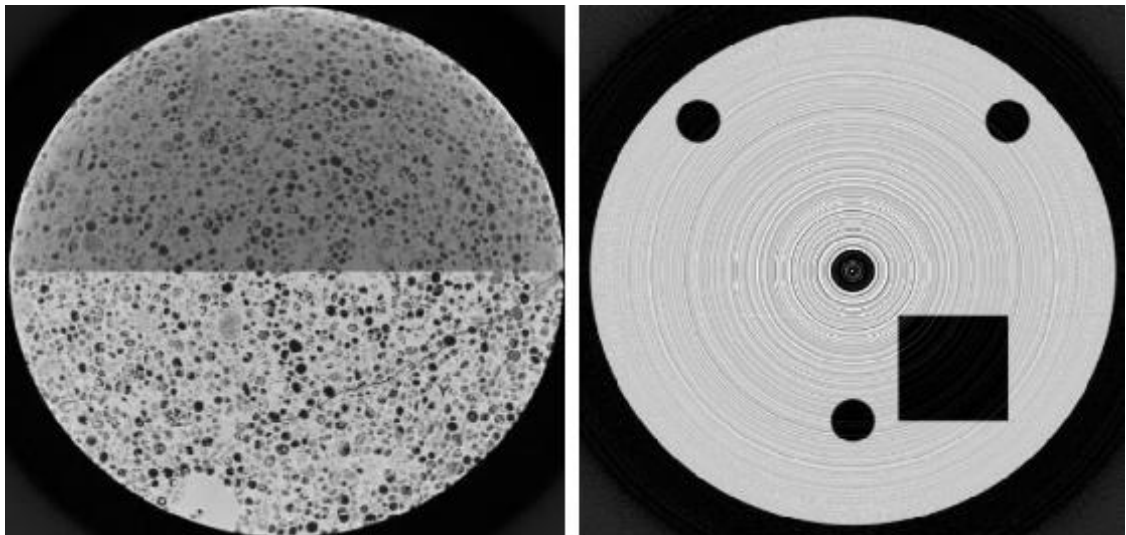


Figure 2.16: Beam hardening and Ring artefacts: (a) Upper level of the picture has no hardening corrections and lower level is after hardening corrections (b) Ring artefacts [70].

A ring artefact is the other common artefact that is produced by local defects in the detection device. Defects in the scintillator or other devices generate continuously erroneous readings at each rotational scanning angle, and appear as a ring. The level of reinforcement increases from the edge to the centre of the specimen. Ring artefacts can be removed by scanner calibration and software corrections [74].

2.3 Summary

During aluminium casting, the liquid aluminium is highly reactive with oxygen and generates an aluminium oxide film in the mould within milliseconds. These oxide films are often responsible for the failure of castings. If the filling velocity is faster than 0.5 ms^{-1} , the turbulent flow generates more oxide films, which are composed of two thin oxide layers that trap air between them by folding. Such oxide layers are called bifilms. Entrained films are thin enough to be furled by turbulent flow during the filling process. It is thought that a furled, thin bifilm may be unfurled by the four main factors of hydrogen precipitation, dendrite pushing, shrinkage and inclusion. However, there is no experimental evidence for this unfurling phenomenon.

A non-destructive method based on micrometer size-resolution measurements is required to observe this unfurling phenomenon. Micro X-ray tomography is a suitable technique because the micrometer-scale X-ray scanning resolution, with its 3-D reconstruction ability, is sufficient for observations of the defects in the specimens from various viewpoints. For the best results, the spatial resolution size should be as small as possible in order to minimize the noise signals and artefacts. To achieve the best conditions, it is important to use the smallest specimen with a cylindrical shape, a longer X-ray exposure time, a smaller rotation step angle and artefact corrections in the reconstruction program.

The unfurling phenomenon is important because it can affect and reduce the mechanical properties. The unfurling phenomenon causes the bifilm to grow larger than its initial size, and the larger size of the bifilm should have a greater negative effect on the mechanical

properties. The objectives of the series of experiments reported are as follows:

1. To establish an experimental method for producing aluminium oxide in a mould and capturing these oxides in cylindrical specimens,
2. To optimise the parameters of a 3-D micro-X-ray tomography technique for different-diameter cylindrical specimens in order to obtain the most realistic 3-D representations of oxide shape and structure,
3. To develop a re-melting technique to facilitate the controlled holding of bifilm defects in a liquid aluminium alloy for different times, and
4. To utilise the above methods to observe the changes that occur in bifilm morphology and the differences between the re-melted specimens and initial oxide shapes.

Chapter 3

Experiment Procedure

3.1 Materials

Commercial aluminium 2L99 was used for this experiment and its chemical composition is listed in Table 3.1.

Table 3.1: Chemical elements of Aluminium alloy.

2L99	Si	Mg	Fe	Mn	Ni	Ti	Be
	7.03	0.36	0.08	0.01	0.01	0.13	0.0012

3.2 Oxide Generation in the Mould and Specimen Preparation

3.2.1 Mould Design

To attain reasonable tomography resolution (less than 5- μ m voxels) with the 3-D X-ray micro tomography equipment (SKYSCAN 1072), the bifilm defects needed to be contained in specimens with diameters of less than 5 mm. A casting technique was developed to make 5-mm diameter specimens containing bifilms. A gravity-filled, chemically bonded sand casting route was selected. The sprue was square (to avoid vortex generation) and tapered, with a top dimension of 30 mm x 30 mm and a bottom dimension of 30 mm x 15 mm (height 200 mm). To minimise oxide generation during pouring and remove oxides in the ingot material, a basin conforming to the specifications of Campbell and a 50 mm x 50 mm x 20 mm 10 pores per inch (ppi) ceramic foam filter (Foseco Sivex FC) were used [30]. To generate oxides inside the mould, an ‘oxide generator’ was used to initiate a hydraulic jump [75]. A 2-mm

3.2.3 Sand Mould

The sand used for the mould was Chelford HST60 with Ashland Pepset Resin 5112 and 5230 (ratio of resins, 1:1). The amount of each resin added was 0.6% of the sand weight, and each component was mixed for 1 minute. The core was removed from the tool 15 to 20 minutes after the cold box was filled with the sand mix.

3.2.4 Real Time X-ray Observation of Mould Filling

A series of castings were poured using a numerically controlled pouring system and the flow was imaged using real-time flow radiography. The details of this method have been reported elsewhere [76]. To pour the liquid aluminium into the mould, a crucible manipulator was used at the full pouring speed. After the crucible location on the robot arm reached a temperature of 750 °C, there was a delay of 17 seconds before pouring. Real time X-ray flow imaging was used to observe the in-mould flow behaviour, along with the defect formation and transport. The specifications for this real time X-ray imaging are listed in Table 3.2.

Table 3.2: The conditions of the real time X-ray machine.

X-ray Condition	Voltage:	120~140 kV
	Amperage:	4.5~7.1 mA
Image Intensifier	Magnification:	1
Video Recording	Frame Rate:	60 fps
	Shutter Speed:	1 X
	Exposure Time:	16666 µsec
	Live Resolution:	Full Frame (800 X 600)

3.2.5 Locating Oxide Defect and Specimen Preparation

After casting, the surface of each specimen was cleaned with sandpaper to remove the sand spots and rough surfaces and two orthogonal X-ray films were taken of each test bar. The X-ray film images were taken with the bar rotated through 90 degrees about its longitudinal axis. The conditions for these X-ray shots followed the British Standard: BSEN 12681. If there was a defect on a film and no defects in the other films at the same height, it was assumed that the defect was on the surface of the specimen. By measuring the defect positions from the center of a specimen, the locations of the defects were determined. Defects located in the center of specimens within 3, 4, 5 and 8-mm diameters were machined to round samples using a lathe.

3.3 3-D Micro X-ray Tomography Set- up

3.3.1 X-ray Tomography Scanning Set-up

For bifilm scanning, microtomography equipment (Skyscan 1072 desktop X-ray Microtomography) was used in this study. Skyscan 1072 consists of a microfocus X-ray tube, high voltage power supply (20–100 kV), specimen stage, precision manipulator, CCD camera (1024 X 1024 pixels), computer and colour monitor (Figure 3.2, left) [72]. The specimen stage can rotate the specimen and adjust the distance between the specimen and X-ray source. X-rays that passed through the specimen were collected by a CCD camera viewing an X-ray scintillator screen for selected exposure times. Scans were performed using the rotation step angles of 0.9 and 0.45 degrees and an object rotation angle of 180 degrees to determine the

optimum scanning conditions. Each image was saved as a '*.tif' file. To determine the optimum conditions, several different scanning conditions were used in this experiment. The scan settings were as detailed in Table 3.3.

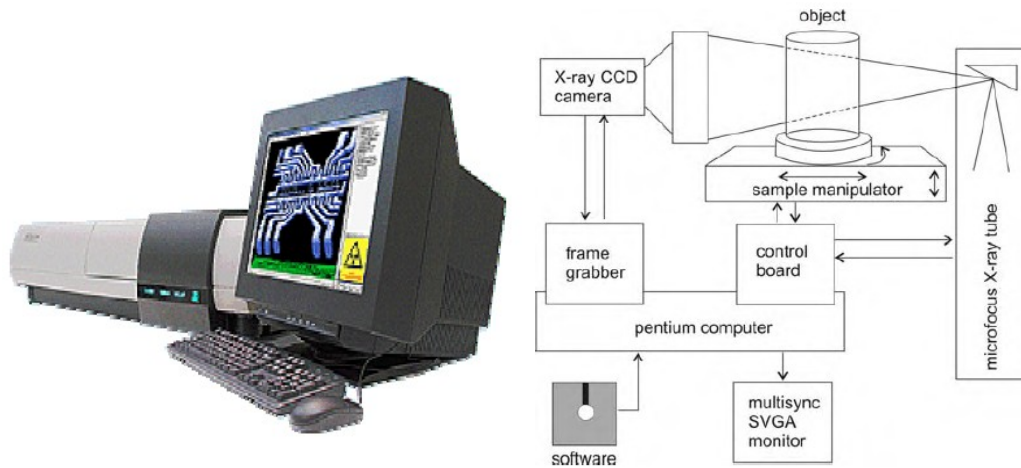


Figure 3.2: Skyscan 1702 (left)([www. Skyscan.be](http://www.Skyscan.be)) and schematic of the scanning system (right) [77].

Table 3.3 Optimum conditions of tomography scanning.

Power and Ampere	100 kV and 96 μ A
Magnification	depending on the size of specimens (3, 4, 5 and 8 mm)
Rotation angle	180 degrees
Rotation step angle	0.90 and 0.45 degrees
Exposure time	2, 5, 7 and 10 sec per scan
Filter	1 mm aluminium filter

After the best settings were determined, all of the scans for the 3, 4, 5 and 8-mm diameter specimens were performed using 0.90 and 0.45 degree rotation step angles with a 180 degree rotation angle. The exposure time was 10 seconds (maximum exposure time in Skyscan 1072). An aluminum filter was used for every scan. The level of magnification was

determined by the FOV. A specimen was moved until it fully filled in the FOV. During this magnification, if any part of the specimen was out of the FOV during a trial specimen rotation of 90 degrees, the magnification was reduced. Since the spatial resolution was adjusted by the magnification, it was important to have the highest magnification possible.

Once the size of the specimen was determined, the exposure time (2, 5, 7 and 10 sec per scan) was studied with a 4-mm specimen. In addition, the rotation angle test was performed with 0.90 and 0.45 degree rotation steps. Exposure time and rotation angle tests were performed to optimize the image quality while achieving a feasible and acceptable maximum scanning duration of 3 hours.

3.3.2 2-D to 3-D Reconstruction Set-up

For reconstruction, the program NRecon (Skyscan, Belgium) was used. A plan utilising a maximum of 974 sections (ranging from section 24 at the bottom to section 998 at the top, in single step increments) was used. In addition, automatic post alignment and the maximum level of ring artefact reduction (a value of 20) were used for the parameter set-up. However, different beam hardening levels were investigated (0, 20, 50, 70 and 100%).

3.3.3 Volumetric Image Reconstruction Set-up.

ANT visualization software, which is provided by Skyscan in Belgium, was used in this study to build 3-D volumetric images. Various contrast levels (grey code) were used, depending on the scanning conditions (the range was 70 to 140) to determine the best grey code level for

building volumetric images and its effect on the images. Because of the volumetric image file size, the region of interest (ROI) and customized file stocks (depending on the height of the defects) were used for the volumetric images.

3.4 Re-melting Process of Specimens

In order to observe the behaviour of a bifilm in liquid aluminium, a re-melting process was developed. Two techniques were used for this study. After re-melting, the specimens were re-scanned by Skyscan 1072 to observe the shape of the oxides.

3.4.1 Quartz Glass Tube with Argon.

A quartz glass tube (Multi-lab LTD, UK) with an argon environment was used to test the re-melting techniques. The external and internal diameters of this quartz glass tube were 10 and 8 mm, respectively. The pressure of the argon was 273 mbar, which was the maximum amount of gas to prevent an explosion at 750 °C. Before sealing the tube with the argon gas, the aluminium specimen was placed at the centre of the tube. Once the re-melting furnace reached 750 °C, the sealed glass was put into the furnace. The furnace used was produced by Pyro Thermo Furnace. The quartz glass tube was observed at 5 minute intervals until the specimen was fully melted.

3.4.2 Ceramic Mould with Air Environment

The other melting technique that was applied in this experiment was the use of a ceramic mould with an open environment, which is close to many real foundry environments. A

ceramic mould was designed as shown in Figure 3.3. The cylindrical form of the top 25-mm was used to insert and hold specimens, while the bottom of the cylinder was blocked. The internal diameter of this mould was 5 mm and the specimen diameter used was 4 mm, which made it easy to insert specimens into the mould at a temperature 745 °C. The rapid ceramic mould technique [78] was used to produce the ceramic moulds. Once the furnace temperature reached 750 °C, the ceramic mould was put into the furnace for 2 hours to soak the mould at temperature. The specimens were put into the mould for different durations: 1, 1.5, 2, 3, 5, 10, 15, 20 and 30 minutes.

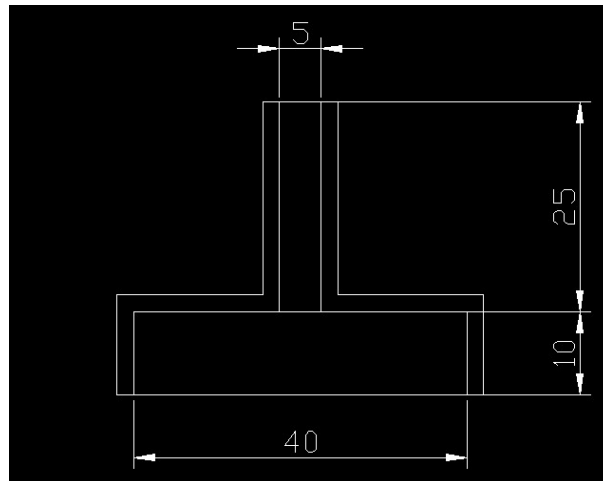


Figure 3.3: A drawing of the re-melting ceramic mould.

3.5 Optical Microscopy

An electronic optical microscope was used to observe the polished surfaces of the cast specimens and the test specimens re-melted for different melting times.

3.6 SEM and EDS

To establish the defect types and the amount of oxide in the cast specimens, scanning electron microscopy (SEM) and energy dispersive X-ray (EDS) observations were made on polished sections. Polished ingot specimens and the portions of the aluminium specimens above the filter were observed before the cast metal passed through the filter. The parts of the specimens that fractured during machining were also observed. After re-melting, the specimens were sectioned, the defects of interest were polished and the oxides were observed to ensure that they were not old films and to determine their chemical behaviour after re-melting. This study used a JEOL 7000 FEG SEM fitted with an Oxford Inca EDS.

Chapter 4

Experimental Results

4.1 Flow Behaviour and Entrainment Oxide in the Mould

Figures 4-1(a) to (f) show real-time X-ray images of the filling process, including images taken from a typical casting, which filled in two seconds. No gas bubbles were observed passing through the ceramic foam filter into the oxide generator. The hydraulic jump structure can be observed at the bottom of the runner (Figures 4-1(d) and (e)). These figures represent the counter-direction flow filling a runner before filling a specimen. Additionally, Figures 4.1(c) and (d) display images of the surface turbulence developed inside the ingate.

Figure 4.2 shows the results for test bars X-rayed using a real-time digital imaging system. There were only two defects detectable in the specimens. These were approximately 1 and 2.5 mm in diameter (circled in Figure 4.2).

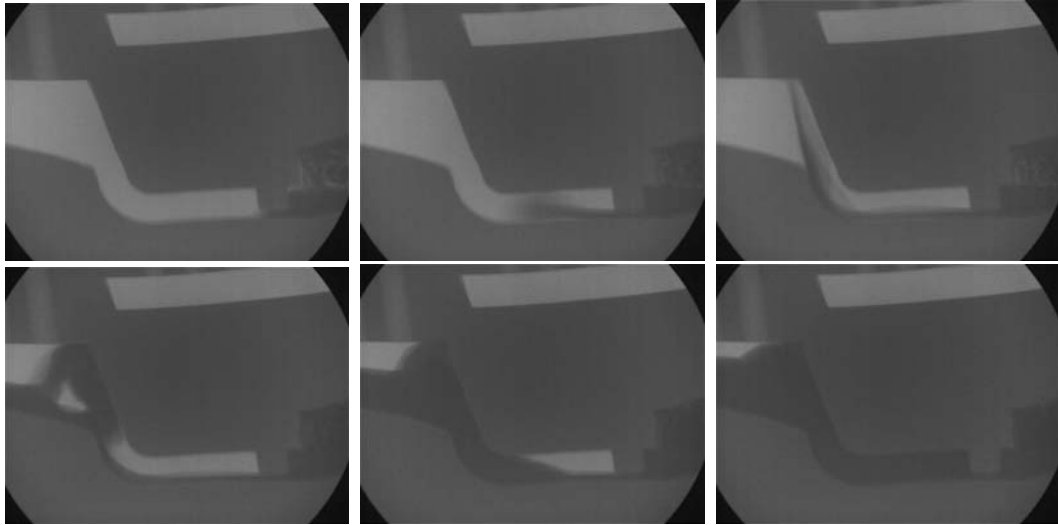


Figure 4.1: Real-time X-ray flow images during the filling process.

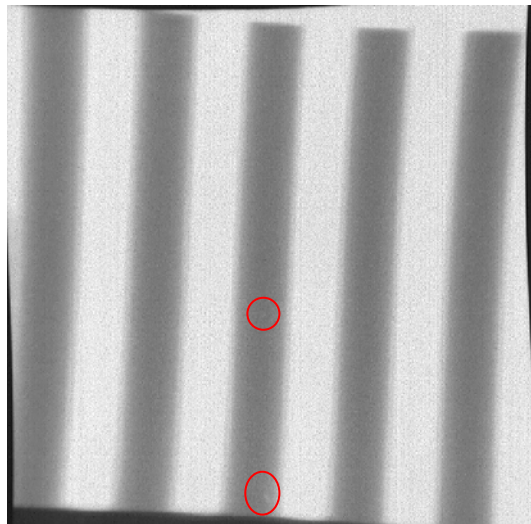


Figure 4.2: Observation of defects using a real-time X-ray machine. Defects of approximately 1 and 2.5 mm diameter are circled.

4.2 X-Ray Film

To improve upon the limited resolution problem of real-time X-ray images, X-ray film was used. Compared with real-time X-rays images, X-ray film images allowed smaller defect

sizes to be observed in casting specimens (Figures 4.3(a) to (d)). General observations of these X-ray film images revealed that most of the defects were distributed near the tops of the specimens (Figure 4.3). In a comparison of 0- and 90-degree X-ray images, some defects appeared in only one image, not both (Figures 4.3(a) and (b) or (c) and (d)). Some defects that were located in the centre of the specimen in one image were located far from the centre in the other image.

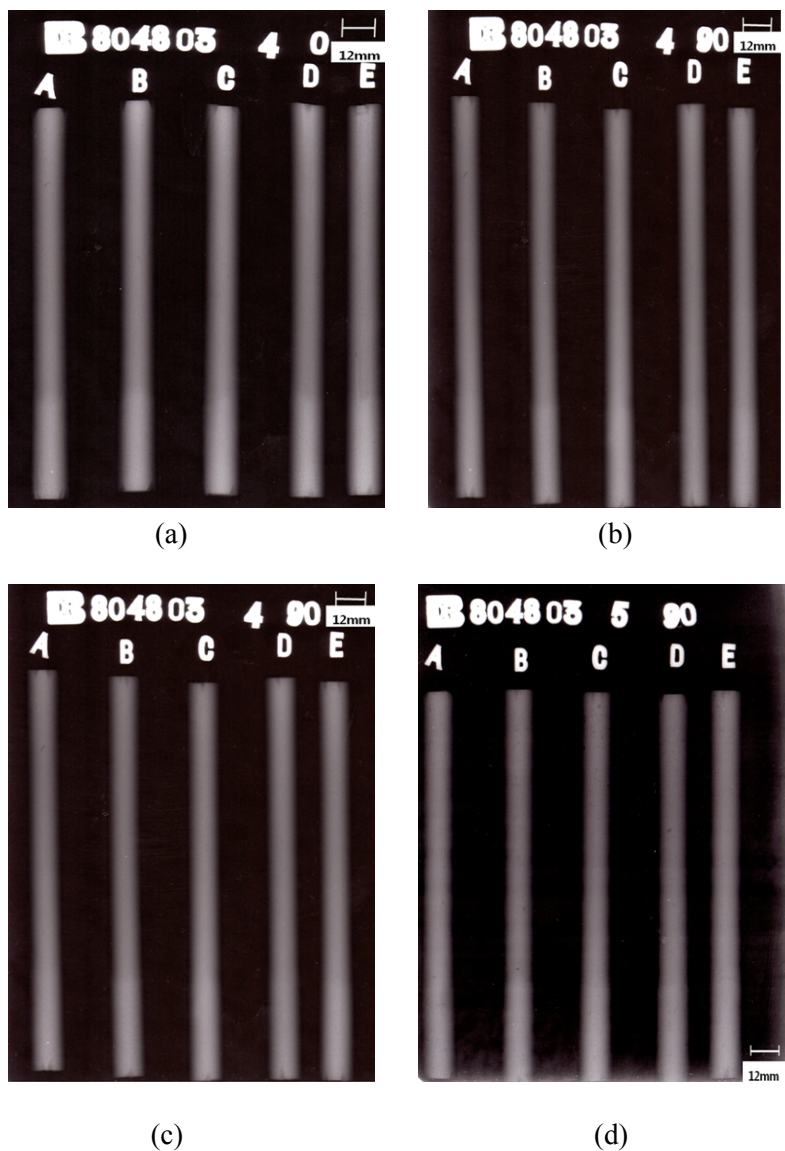


Figure 4.3: Film X-rays of 12mm diameter casting specimens before machining observed at two different orientations: 0° (left) and 90° (right).

After machining the specimens, the positions of the defects were near the surfaces of the specimens in both images (Figure 4.4).

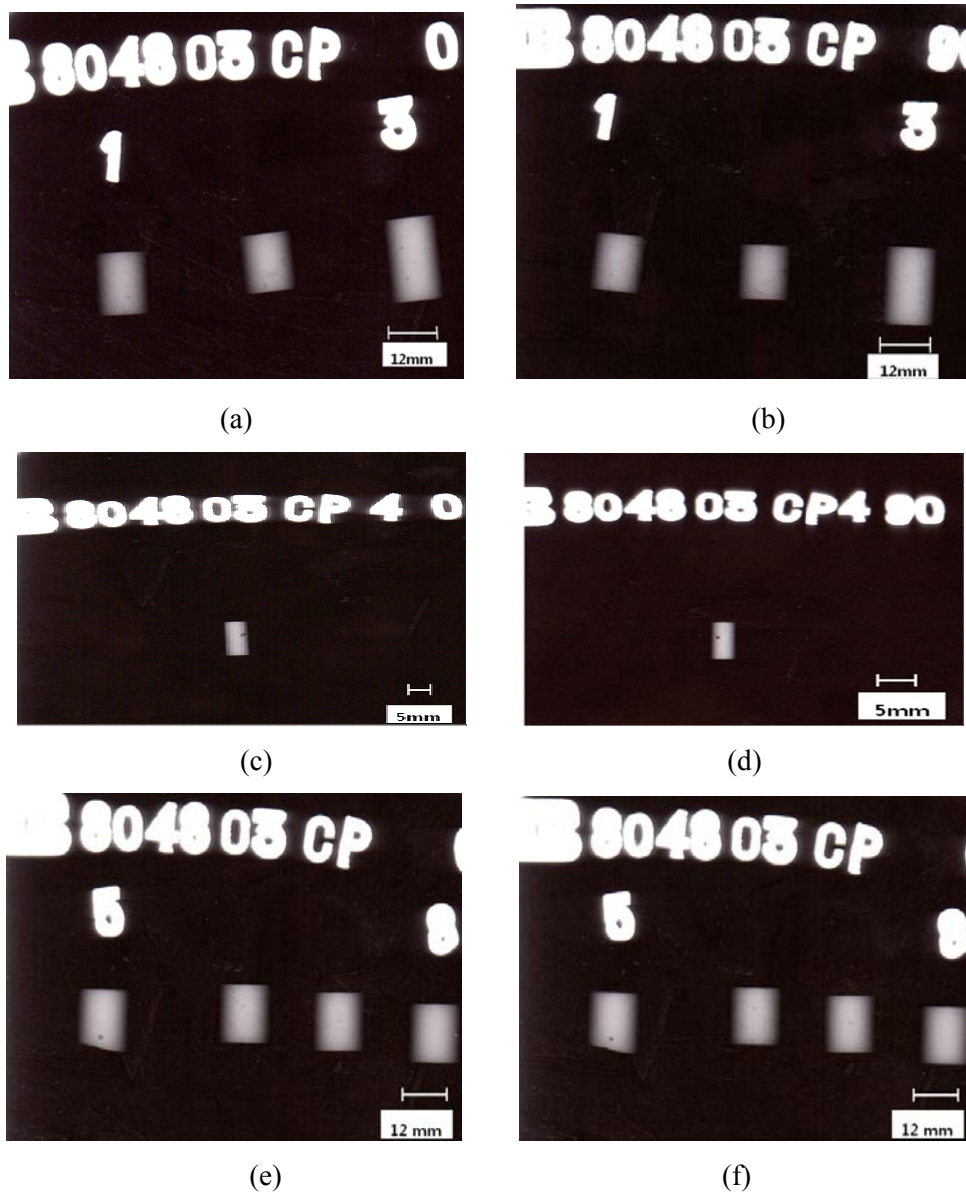


Figure 4.4: X-ray film images from two different angles, 0° (left) and 90° (right), after machining to 8-mm diameter ((a), (b), (e) and (f)) and 5-mm diameter ((c) and (d)).

4.3 Metallographic Imaging of Film X-Ray Defects

The ability of the film technique to detect bifilm filling defects was confirmed by

metallography (Figures 4.5 and 4.7). Most defects had complicated geometric structures consisting of bubbles and thin, double layers of oxide (see Figures 4.5 and 4.7). The linear dimensions of the oxide defects were as large as 1.5 mm, and they commonly developed trapped gas bubbles. The bifilms were separated by air gaps of 2 μm to 20 μm (see Figures 4.5 and 4.7). It was easy to determine that bifilms were always associated with eutectic phases, as shown in Figures 4.6(c) and 4.7(b).

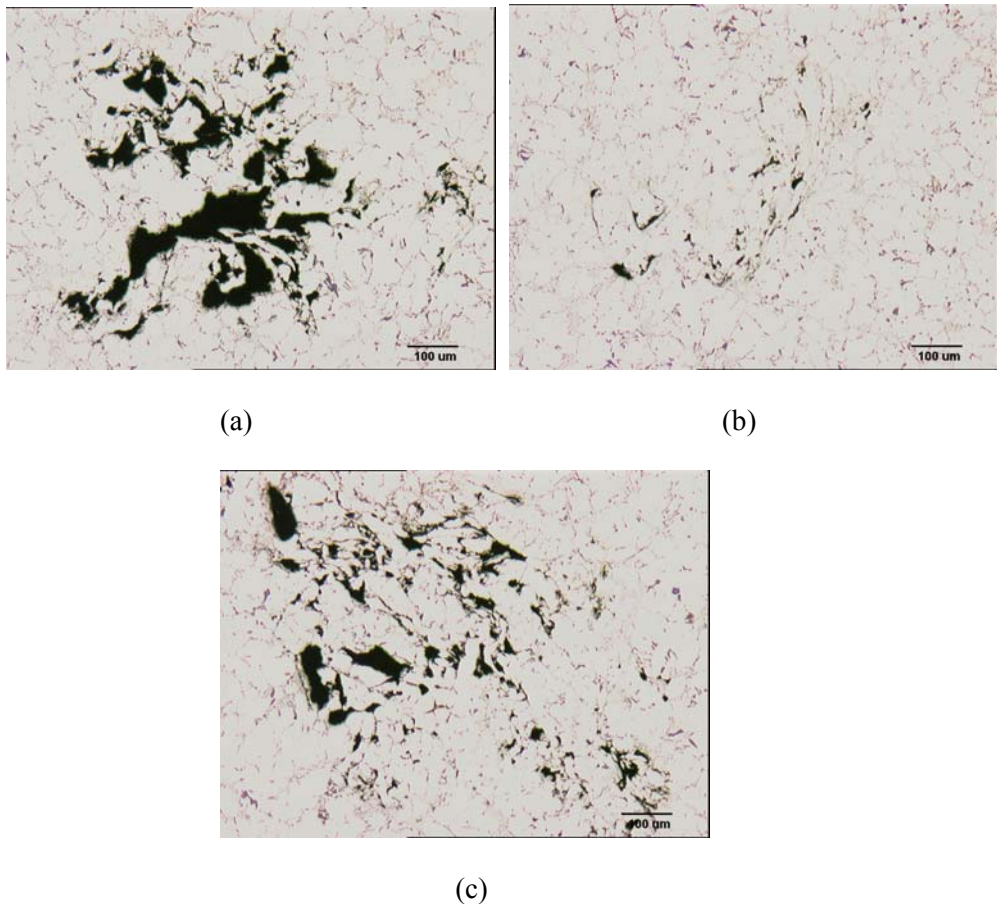


Figure 4.5: Metallographic sections through defects in the X-rays of Figures 4.3 and 4.4: (a) gas hole structures with oxides, (b) small gas hole structure with thin double oxide layers and (c) gas holes with thin double oxide layers that were tangled together.

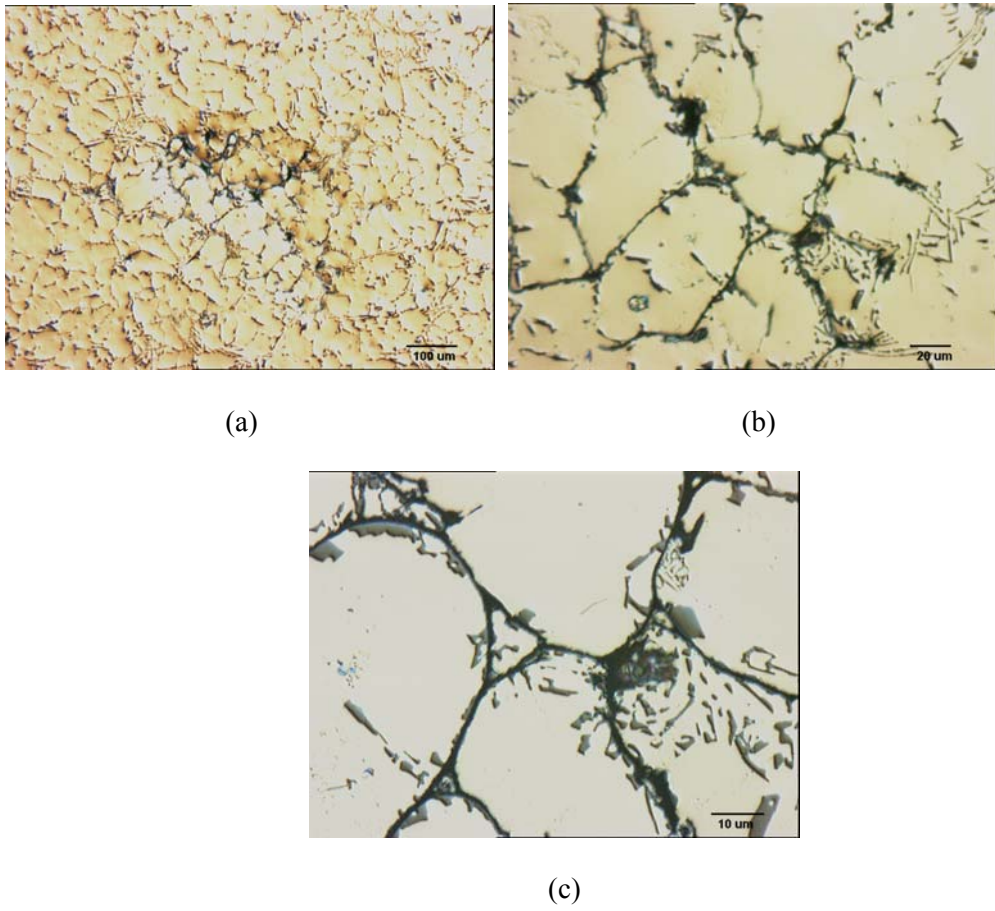


Figure 4.6: Different magnifications of oxide films that were detected after polishing but not identified on the X-ray film.

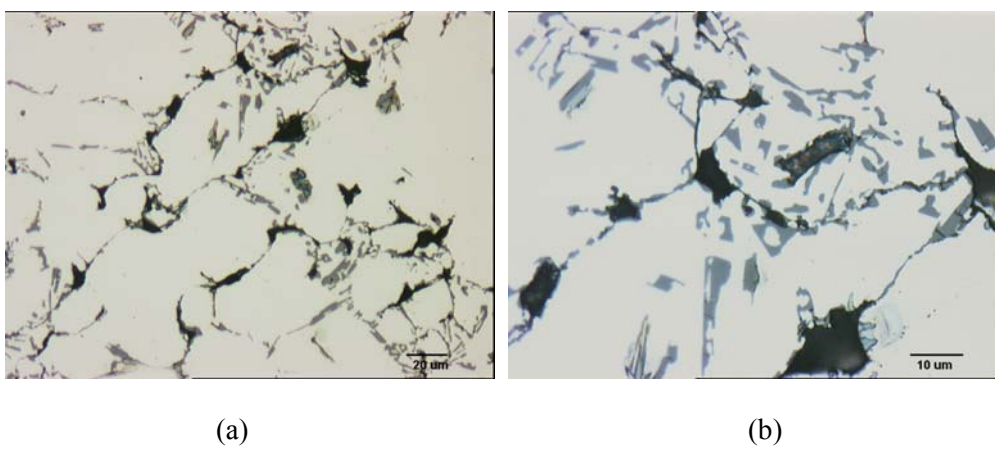


Figure 4.7: Different magnifications of bifilms that were detected after polishing but not identified on the X-ray film.

4.4 SEM and EDS Results for Ingot and Casting Specimens (before re-melting) and Fractured Surfaces Caused by Machining

4.4.1 SEM and EDS Results of Ingot

The ingot specimens showed many defects containing young and old oxides, shrinkage porosity and intermetallics (Figure 4.8(a)). Many thick, crusty, untangled oxides (i.e. old oxides) were observed inside the defects (Figure 4.8(b)). The EDX results indicated that the oxygen levels of features resembling oxides ranged from 30 wt% to 40 wt% (Figures 4.8(c) and (d)).

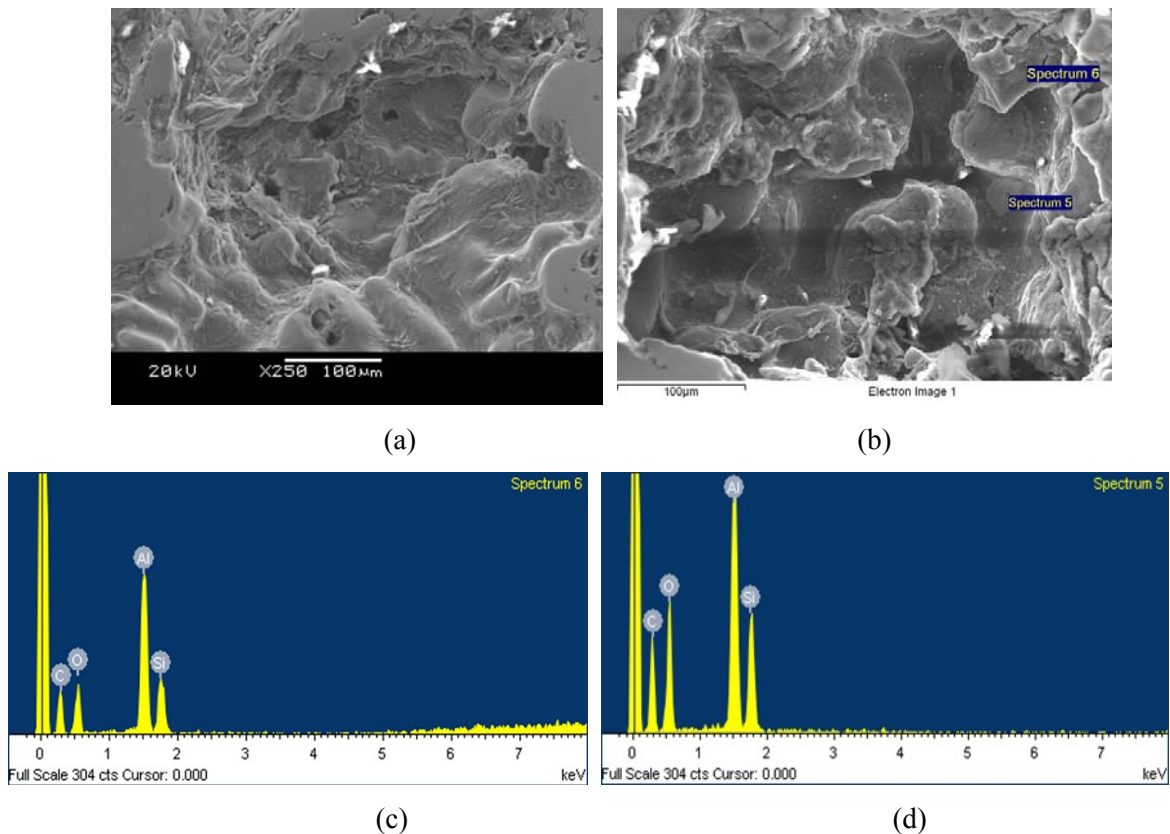


Figure 4.8: SEM images ((a) and (b)) and EDS analysis ((c) and (d)) of old oxide found within ingot samples.

4.4.2 SEM and EDS Results of Casting Specimens

Figures 4.10 and 4.11 show images of young oxide films in casting specimens. A thin, tangled oxide film fully covers the internal surfaces of the defect in Figure 4.9. Shrinkage porosity associated with oxide films was also observed; an example is shown in Figure 4.10(a). A higher magnification view (Figure 4.10(b)) (with indicated EDS analysis points) shows the aluminium oxide film (5.53 wt% oxygen) in Figure 4.10(c) and aluminium (100 wt%) in Figure 4.10(d).

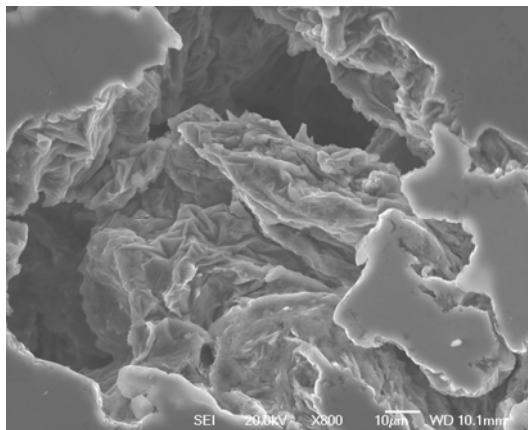


Figure 4.9: Young oxides in an aluminium casting specimen

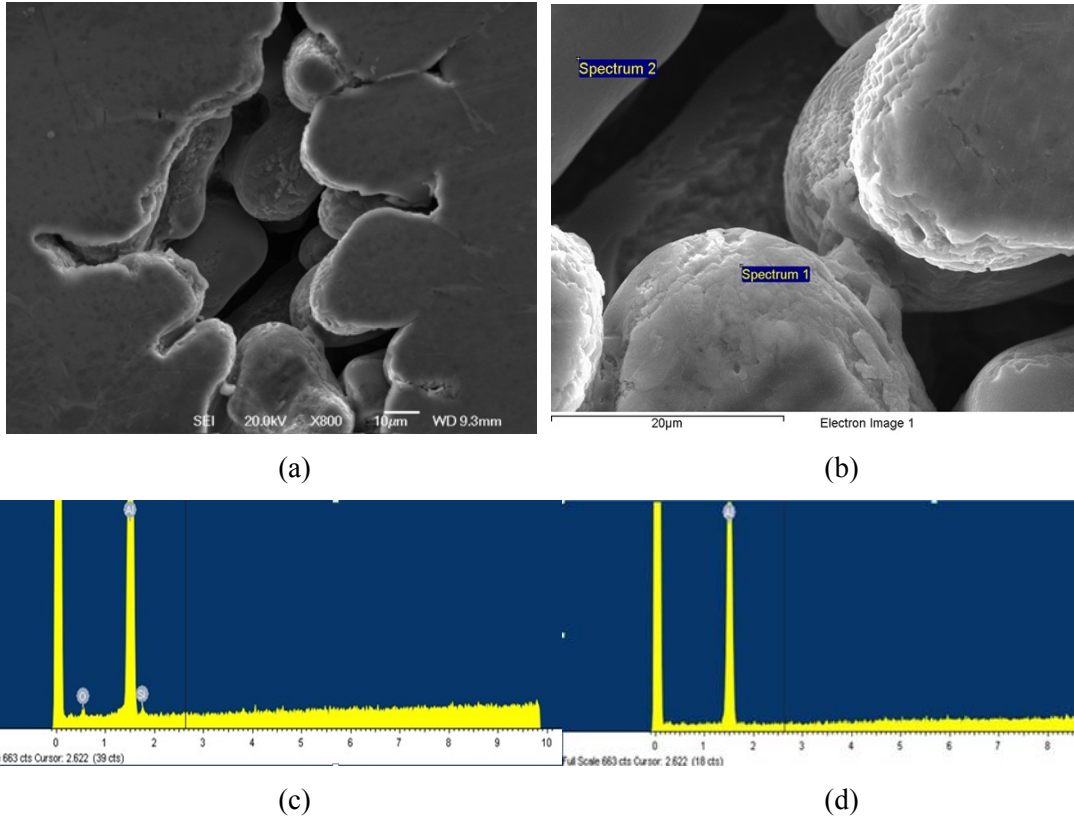


Figure 4.10: Shrinkage porosity of oxide layers in the casting specimens: (a) and (b) shrinkage porosity with oxide, (c) Al 100 shrinkage porosity with thin oxide layers (O_2 5.53 wt%) and (d) shrinkage porosity with pure aluminium(%).

4.4.3 Fractured Test Piece Surfaces.

Through SEM and EDS observations of samples fractured during machining, it was determined that the failures were caused by oxide layers and shrinkage pores. In Figure 4.11(a), the failure during machining initiated from a large shrinkage pore that extended across much of the surface and was connected to an oxide film. In the centre of the shrinkage pore (Figure 4.11(b)), there were pieces of oxide (inside the red circle), which had not been observed on any other surfaces, and a layer of oxide could be observed at the bottom part of the pore (Figure 4.11(c)). A normal brittle fracture through Si eutectic phase cleavage can also be observed in Figure 4.11(c). Observation of the oxide under high magnification

revealed that the oxide was comprised of thin wrinkled films (Figure 4.11(d)), and an EDS analysis showed that the oxygen peak was less pronounced than the oxygen peaks obtained from the oxides in the ingots (Figure 4.11(e)).

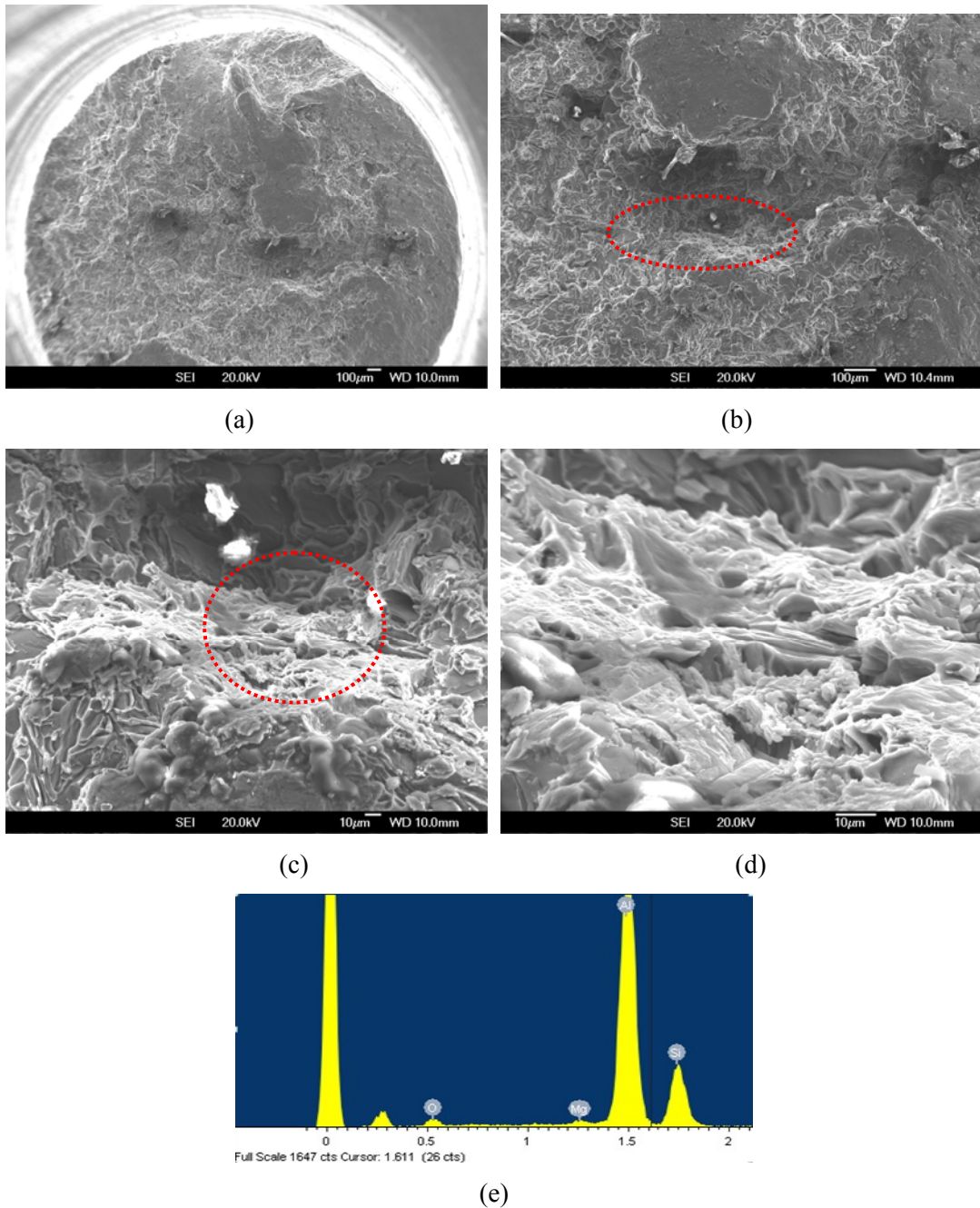


Figure 4.11: (a) - (d) SEM and (e) EDS images of fracture surfaces with porosity showing reduced oxygen signal.

Another specimen, shown in Figure 4.12(a), displayed a fracture that initiated from the defect in the centre of the specimen. Through observations of both sides of the normal brittle fracture in the Si eutectic phase, it was discovered that the young oxide film (the thin and wrinkled film shown in Figure 4.12(c)) covered nearly the entire fracture surface. EDS analysis showed oxygen levels that were lower than those of the old oxides found in the ingots.

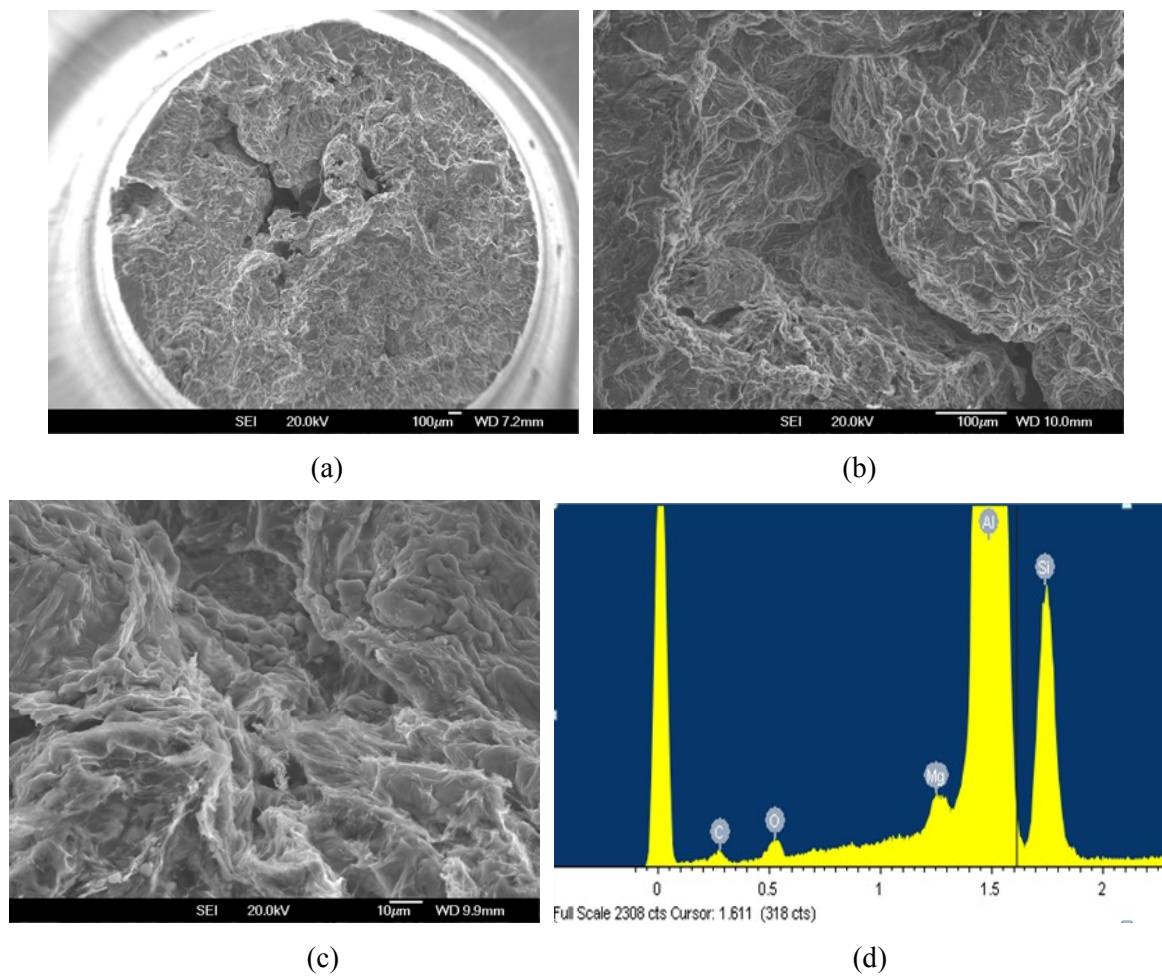


Figure 4.12: SEM images (a) to (c) and EDS analysis (d) a surface of fractured during machining with young oxide.

4.5 Micro-focus X-ray tomography

4.5.1 Relationship Between Spatial Resolution and Specimen Sizes

To determine the casting specimen size that would be best for scanning, specimens of different diameters were tested. The spatial resolution depended on the magnification and the field of view (FOV). The FOV occupied a full section of the screen in the volumetric reconstruction program. The sizes of the specimens were determined by their minimum machining abilities. Specimens less than 3 mm in diameter broke easily, and only a few specimens with 3-mm diameters could be created. The limited accuracy of the machining method, however, produced specimens with irregular diameters of 3 ± 0.2 mm. Therefore, the magnification of the 3-mm diameter specimens could not be greater than 54.59 times (for a spatial resolution of $5 \mu\text{m}/\text{voxel}$) because samples that had diameters of nearly 3.2 mm were out of the FOV. Specimens that were 4, 5 and 6 mm in diameter also had the same spatial-resolution limitations as the 3-mm diameter specimens. The minimum spatial resolutions and magnifications for specimens of different diameters are presented in Table 4.1. The other problem with the 3-mm diameter specimens was that many were broken during machining. Eventually, it was decided that 4 mm was the minimum diameter that could be machined and still produce a reasonable yield.

Table 4.1: Specimen diameter with spatial resolutions and magnifications of Skyscan 1702.

Specimen Diameter	Minimum Spatial Resolution (μm voxel)	Magnification
3mm	5.0	54.59
4mm	5.0	54.59
5mm	6.5	32.29
8mm	11.0	24.83

4.5.2 Data Acquisition Parameters with Different Exposure Times and Rotation Step Angles.

Once the specimen size was set at 4 mm, the best scanning condition needed to be determined. Figure 4.13 illustrates the effect of exposure times of two and seven seconds. When the exposure time was two seconds, it was impossible to produce 3-D images (a). With an exposure time of seven seconds, the targeted oxide with porosity could be observed, but substantial noise was still present (b). When reducing the noise as shown in Figure 4.13, the defect volume was decreased from 0.464 to 0.036 mm³, as seen in Table 4.2.

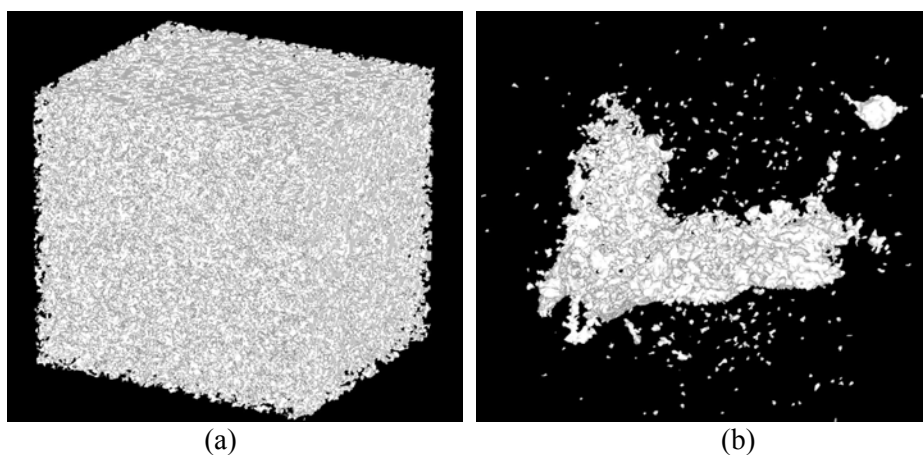


Figure 4.13: 3-D images with different exposure times—(a) 2 and (b) 7 seconds with a rotation step angle of 0.90 degrees and a grey code level of 80

Figure 4.14 shows the benefit of reducing the step angle to 0.45 degrees, as compared to the results obtained with a 0.90 degree step angle (Figure 4.13(c)). The resulting volume increased, as compared to the 7-second scanning result displayed in Table 4.2. When using the 0.45 degree angle, however, the scanning time and data collection more than doubled. The smaller rotation step angle also increased the reconstruction time by increasing the ratio of reducing step angles. The effects of the scanning parameters on the defect volume are shown in Table 4.2.

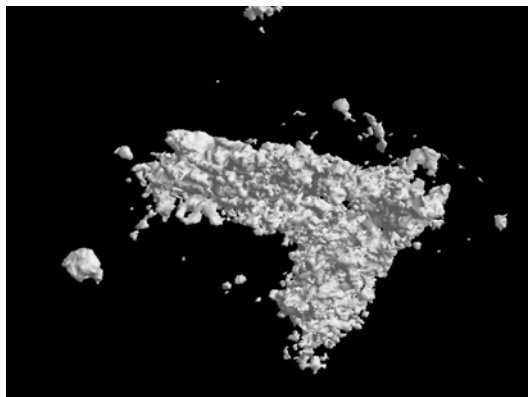


Figure 4.14: 3-D image obtain with an exposure time of ten seconds, a rotation step angle of 0.45° and a grey code level of 80

Table 4.2 Volumes of different rotation step angles and exposure times

Rotation step angle (degree)	exposure time (sec)	Volume (mm ³)
0.9	2	0.464
0.9	7	0.036
0.45	10	0.043

4.6 Image Reconstruction Parameters

Hardening and ring artefacts were the most common artefacts discovered during scanning, but they were controlled during reconstruction. The following section presents the results obtained during the optimisation of the reconstruction parameters.

4.6.1 Hardening Correction Effects.

Figure 4.16 shows the effects of selecting different levels of hardening correction on 4-mm specimens with identical grey codes. When there was no hardening correction (Figure 4.15(a)), the solid parts showed only the defect areas and the surrounding area of the specimen's edges. As the hardening correction level increased to 20%, 50%, 70% and 100%, the solid (red and black) areas increased in the centres of the specimens. The volume of the targeted objects also increased as the correction level increased, as seen in Table 4.3. During the correction, the volume increased slowly until correction level 20; after that level, the volume increased rapidly.

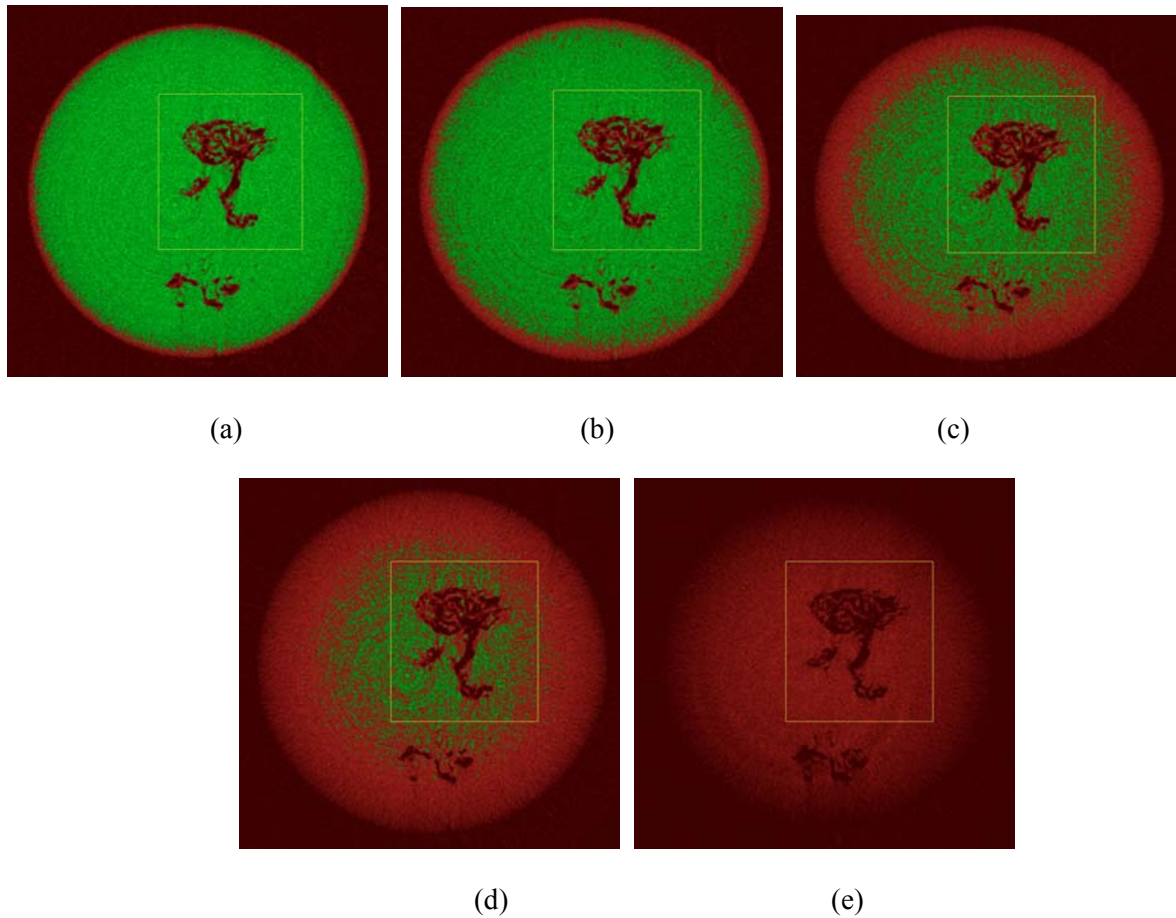


Figure 4.15: Volumetric reconstructed images with a binary grey code value of 130 (threshold value): (a) no hardening correction with no ring artefact correction, (b) 20% hardening correction, (c) 50% hardening correction, (d) 70% hardening correction and (e) 100% hardening correction.

Table 4.3 Hardening correction level and volume of the targeted defects.

hardening correction	Volume of the defect
0	0.188
20	0.243
50	0.745
70	1.738
100	3.123

4.6.2 Ring Artefact Correction

Figure 4.16 shows the effects of different correction levels for ring artefact correction. Before ring artefact correction (Figure 4.16(a)), blurring could be seen clearly. The blurring was

reduced as the correction level increased (from 0 to 20, in 5 unit steps). The best setting was level 20.

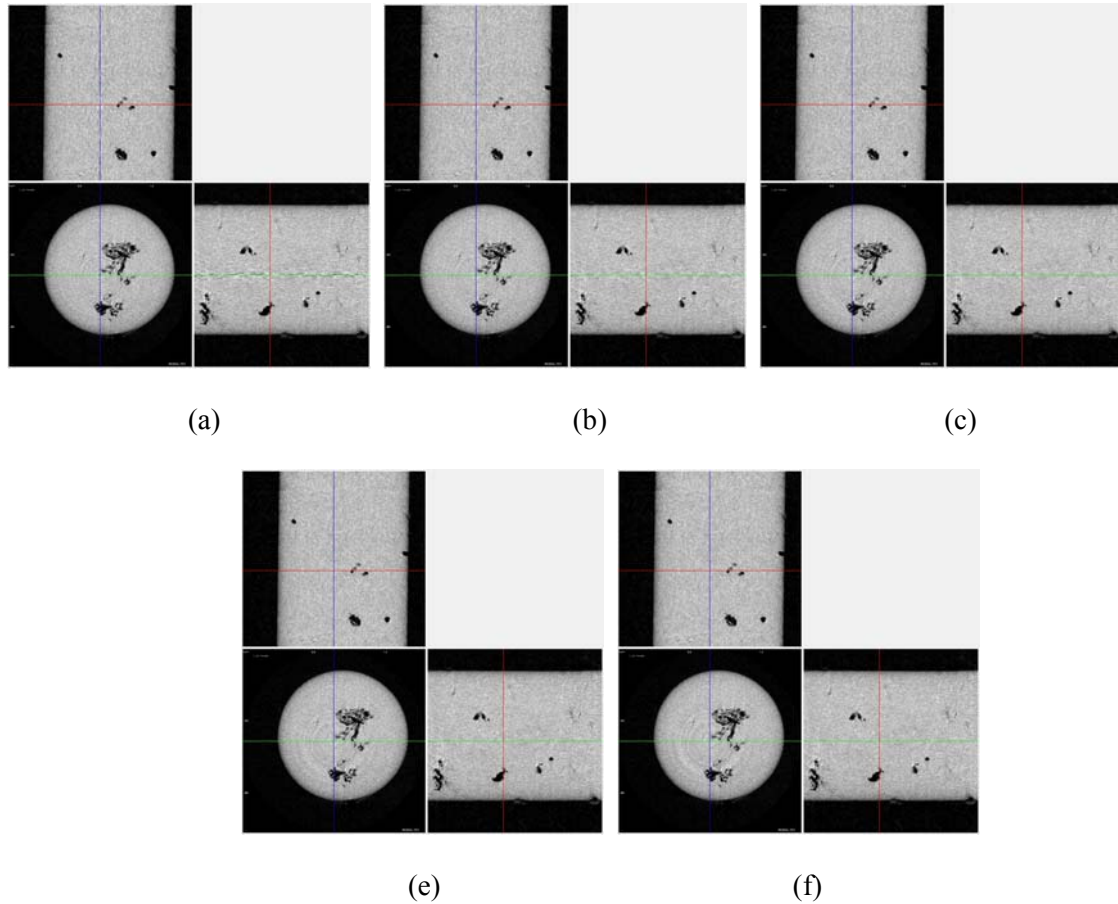


Figure 4.16: Different ring artefact correction levels: images with three different sections (the lines indicate where blurring occurs) at correction levels (a) 0, (b) 5, (c) 10, (d) 15, and (e) 20.

4.7 Volumetric Images

4.7.1 Threshold Effect on Volumetric Images

During the building of the 3-D volumetric images, some grey code-level errors needed to be resolved. Inside the defects depicted in the X-ray images shown in Figures 4.17(a) and (c),

there were some solid structures (indicated by arrows) that did not appear solid. The cross-sections of the 3-D volumetric images (Figures 4.17(b) and (d)) clearly show that no internal structures can be seen in the X-ray images. The volume changes, with different threshold levels, are presented in Table 4.4. The volume rapidly increased when the thresholds decreased from 160 to 140, and there were significant noise reductions. When the threshold level decreased from 140 to 70, however, the volume slowly decreased, and details of the targeted object became less clear.

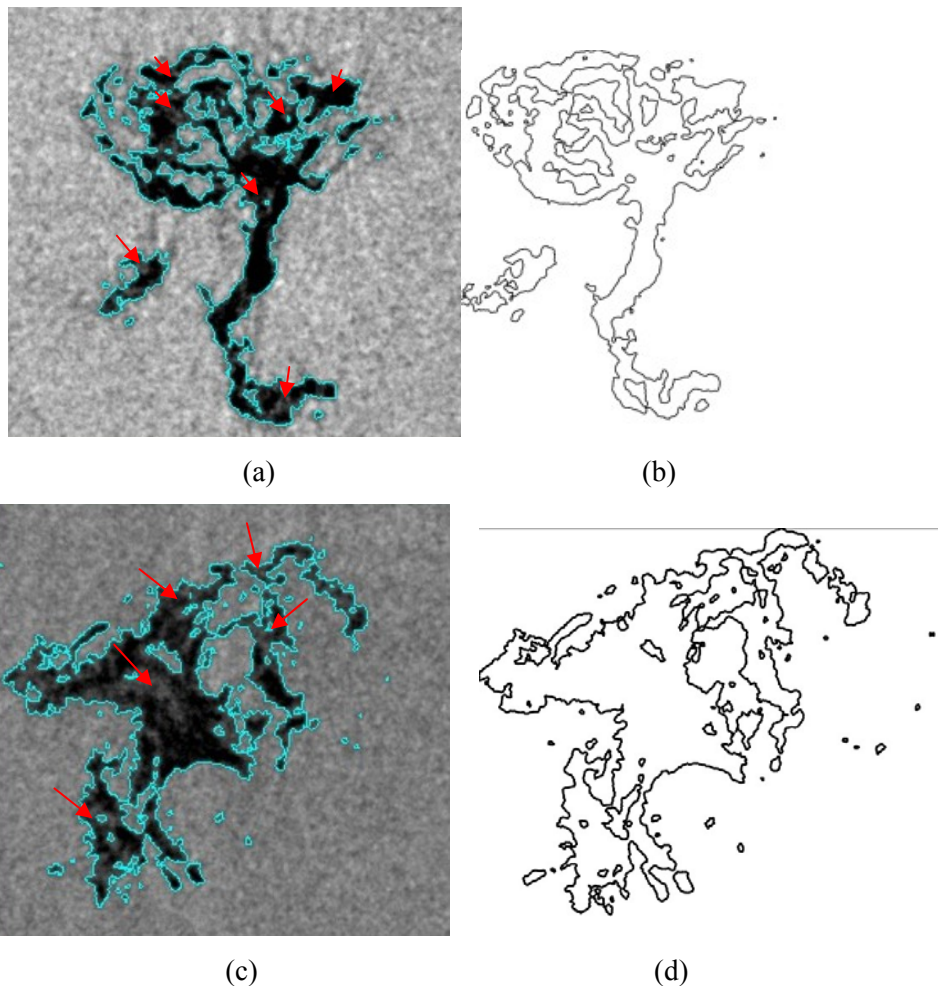


Figure 4.17: Reconstructed X-ray microimages indicating the volumetric image area ((a) and (c)) and cross sections from 3-D images, including the volumetric selection area ((b) and (d)).

Table 4.4 Effect of threshold level on the volume result of target object.

Threshold level	Volume of a defect (mm ³)
160	0.368
150	0.259
140	0.210
130	0.183
120	0.163
110	0.146
100	0.130
90	0.115
80	0.102
70	0.090

4.7.2 3-D Images of Pores with Aluminium Oxides

Pores associated with oxides in a casting of A356 alloy, visualized as 3-D images, are shown in Figure 4.18. These images were generated with 5.0- μm size voxel data sets that were obtained using ten-second exposure times and 0.45 degree rotation step angles. No hardening effects or maximum ring artefact corrections were used for the reconstructions. The range of the maximum defect lengths was between 1.10 and 2.114 mm (each individual length is reported in Figure 4.18). The results for the number of defects per volume and the volume of the targeted defects are displayed in Table 4.5.

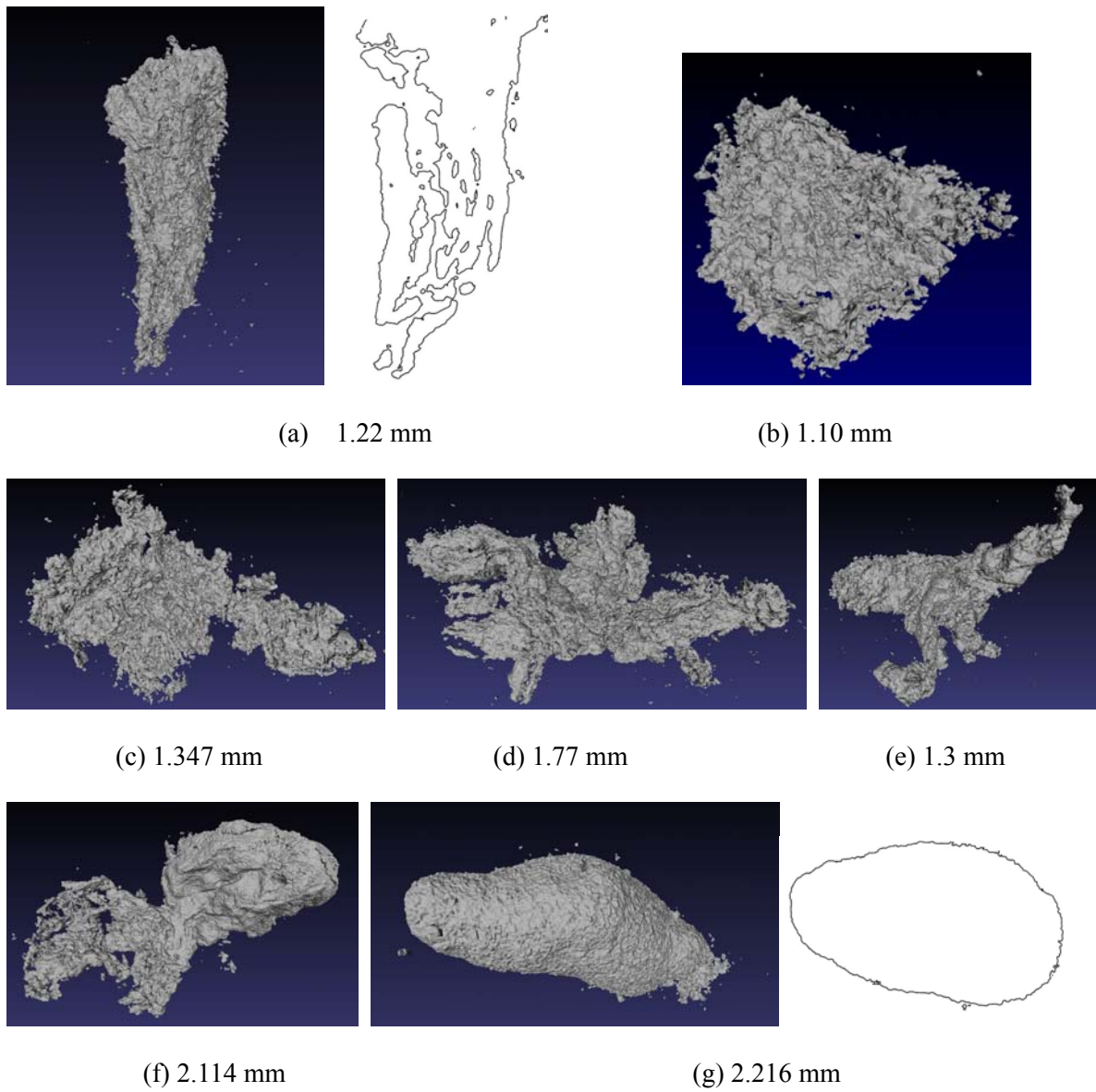


Figure 4.18: 3-D volumetric images before re-melting, including cross-section views: (a) 3 mm, sp1; (b) 4 mm, sp1; (c) 4 mm, sp2; (d) 4 mm, sp3; (e) 4 mm, sp4; (f) 4 mm, sp5; and (g) 5 mm, sp1; the figure beside each caption identifier denotes the maximum linear defect length.

Table 4.5 The number of defects per unit volume scanned and the volumes of targeted defects.

Specimen ID		Before melting	
		Number of defects per volume (number / mm ³)	Volume of target defect (mm ³)
4 mm	sp1	0.354	0.049
	sp2	0.442	0.186
	sp3	0.378	0.393
	sp4	0.322	0.157
	sp5	0.521	0.451
3 mm	sp1	0.311	0.131
5 mm	sp1	0.234	0.737

4.8 Development of Re-Melting Techniques

4.8.1 Quartz Glass Tube with Argon Sealing

In a melting experiment, in which a quartz glass tube was used at 745 °C, it was observed that the tube could not hold its shape (cylindrical; see Figure 4.19) at such a temperature. Additionally, during the re-melting process, molten aluminium wetted the tube. Pores associated with oxides moved to specimen surfaces. Hence, it was impossible to track individual defects throughout the re-melting procedure. After the intermetallic parts were polished, SEM and EDS results indicated that SiO₂ particles had penetrated and filled the oxide network (Figures 4.20(a) and (b)). The weight percentages of the oxygen and silicon in the intermetallics were 47 wt% and 39.19 wt%, respectively, aligning with their respective atomic percentages of 54.4 atomic% (oxygen) and 25.65 atomic% (silicon).

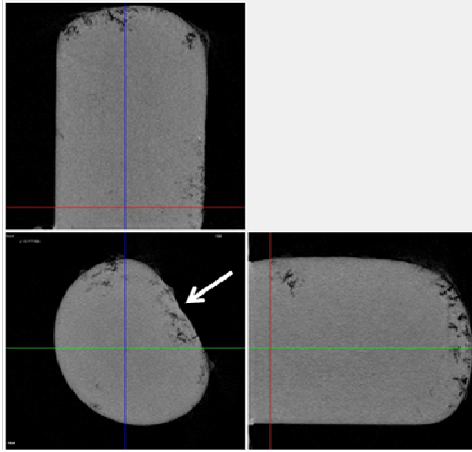
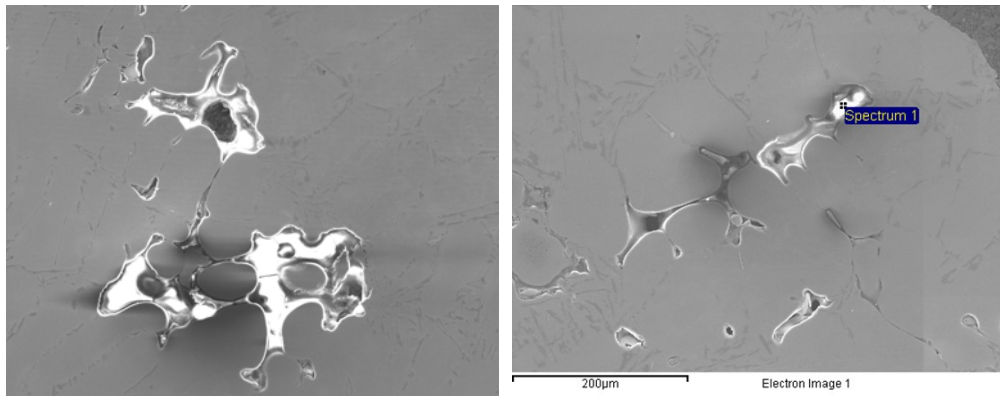
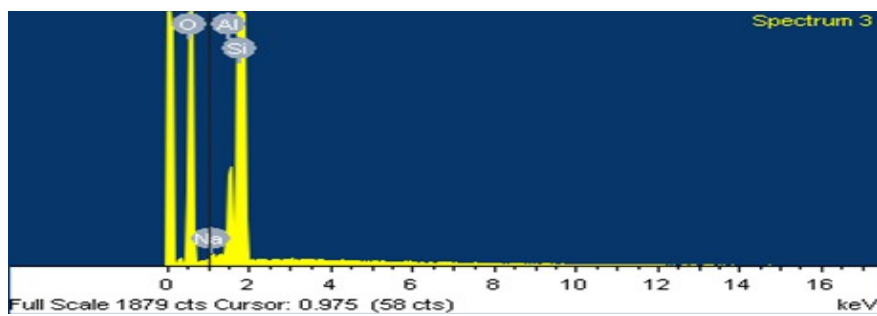


Figure 4.19: Reconstructed X-ray images after melting a quartz glass tube at 750 °C for 40 minutes; the arrow indicates the top of the specimen.



(a)

(b)



(c)

Figure 4.20: SiO_2 particle inclusions, identified after re-melting inside a quartz glass tube: (a) and (b) SEM images of SiO_2 particles with oxide networks and (c) EDS result indicating SiO_2 particles.

4.8.2 Ceramic Mould in an Open Environment

4.8.2.1 Re-Melting with Different Melting Times

Different melting times were tested using 4-mm diameter specimens in order to discover the best melting time (Figure 4.21). Before melting, the test specimens did not have pores larger than 100 μm associated with oxides. Full melting occurred within 1 to 1.5 minutes. The amount of gas porosity did not change significantly, but increases in the size and number of small pores and in the amount of rounded hydrogen pores could be observed after five minutes. After more than ten minutes, gas pores larger than 100 μm could be observed near the edges of the specimens.

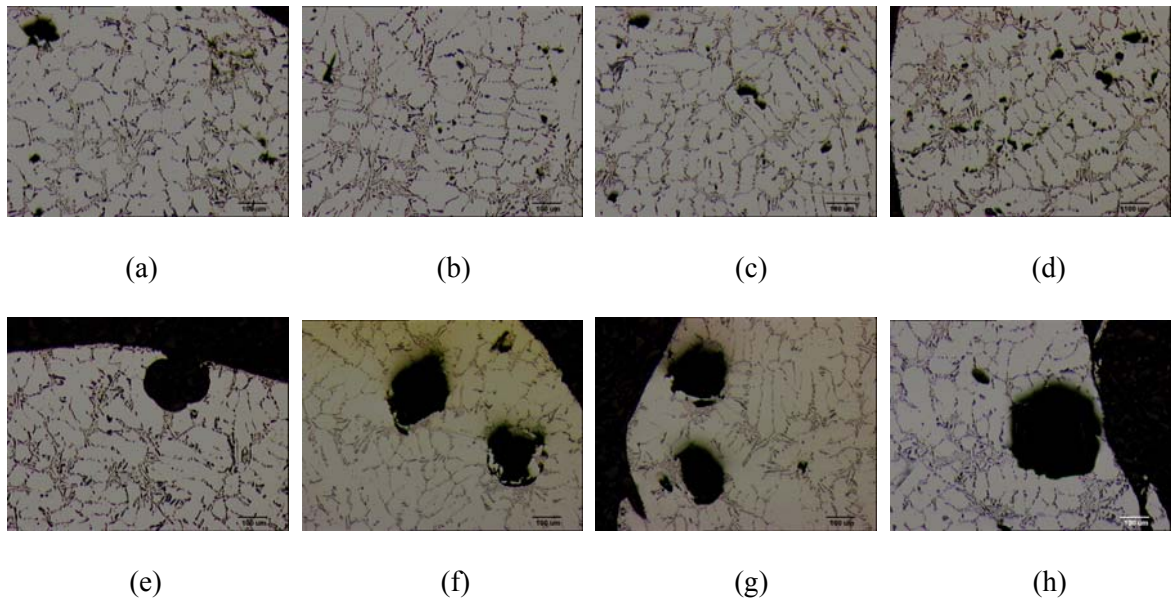


Figure 4.21: Re-melting 4-mm diameter test specimens at 745 °C with different holding times: (a) one minute, (b) two minutes, (c) three minutes, (d) five minutes, (e) 10 minutes, (f) 15 minutes, (g) 20 minutes and (h) 30 minutes.

4.9 Micro Tomography Scanning After Re-Melting

After re-melting was conducted, including air cooling, within a ceramic mould at different melting times of 1, 1.5, 2, 3 and 5 minutes at 745 °C, the specimen shapes changed, with the bottom thickness increasing to a diameter of 5 mm. The top thickness, however, remained at a diameter of 4 mm. The specimens were fully melted after 1 to 1.5 minutes.

Two different defect motions and behaviours could be identified after melting the specimens. First, defects that were connected with a specimen's surface did not change their positions, and their shapes did not change significantly (Figures 4.22, 4.23(a) and 4.18(a)).

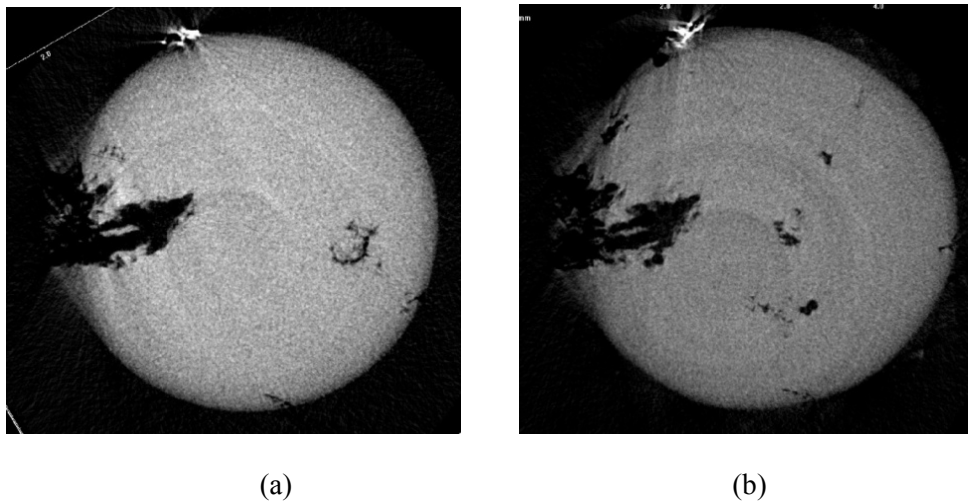


Figure 4.22: Comparing surface connected defect position (a) before and (b) after 5 minutes melting, in a 4mm diameter specimen.

Second, most pores associated with oxides that were in the bulk of the specimens originally either floated or sank. Figures 4.23(b) and (c) show pores associated with oxides at the top and bottom of a specimen, respectively. In Figure 4.23(e), a defect with shrinkage defects can

be found at the top of the specimen. This defect, however, had the same shape as it did prior to melting. The main body of this pore did not change from its initial shape, as seen in Figure 4.22. Except for the pore displayed in Figures 4.23(a) and (e), it was impossible to track pores that were scanned before melting in the centre of specimens because their shapes and positions changed. The number of defects per unit volume and the volume of the targeted pores associated with oxides are presented in Table 4.6. However, because the targeted pores changed their positions and shapes, relatively few oxide volumes could be measured.

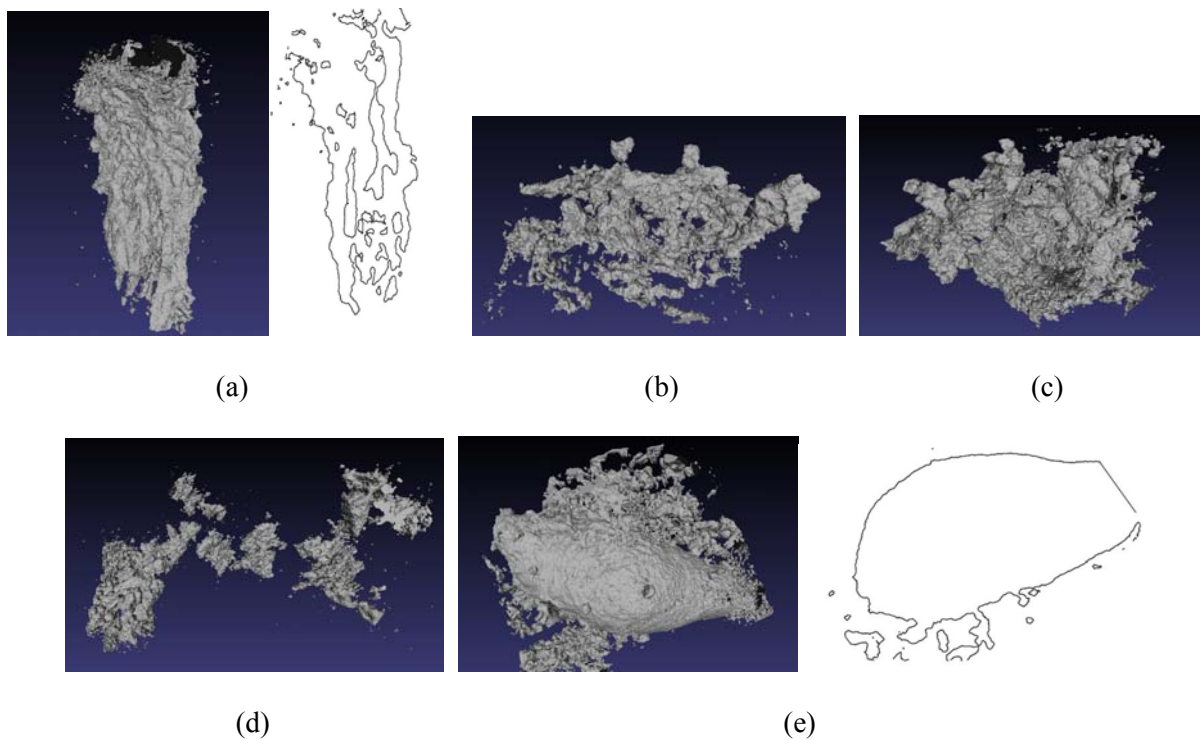


Figure 4.23: Scanned defects, with cross-section images, after re-melting specimens with different melting times: (a) 3-mm diameter specimen for three minutes with a cross-section image, (b) 4-mm diameter specimen for 1.5 minutes, (c) 4-mm diameter specimen for three minutes, (d) 4-mm diameter specimen for five minutes and (e) 5-mm diameter specimen for five minutes.

Table 4.6 Number of defects per volume in specimens and the volume of targeted oxides

Specimen ID		After melting	
		Number of defects per volume (Number/mm ³)	Volume of defect (mm ³)
4 mm	sp1	0.163	N/A
	sp2	0.107	N/A
	sp3	0.147	N/A
	sp4	0.115	0.119
	sp5	0.044	N/A
3 mm	sp1	0.127	0.182
5 mm	sp1	0.048	N/A

4.10 SEM and EDX Oxide Results in Re-Melted Specimens

Figures 4.24 and 4.25 show SEM images of polished sections, viewed through various defect positions. When young oxide films were observed by EDS, only low-oxygen counts were measured (Figure 4.24(c) and Figure 4.25(d)). The tangled defect in Figure 4.25 shows that pure aluminium was present between double oxide layers that had complex convoluted oxide network shapes.

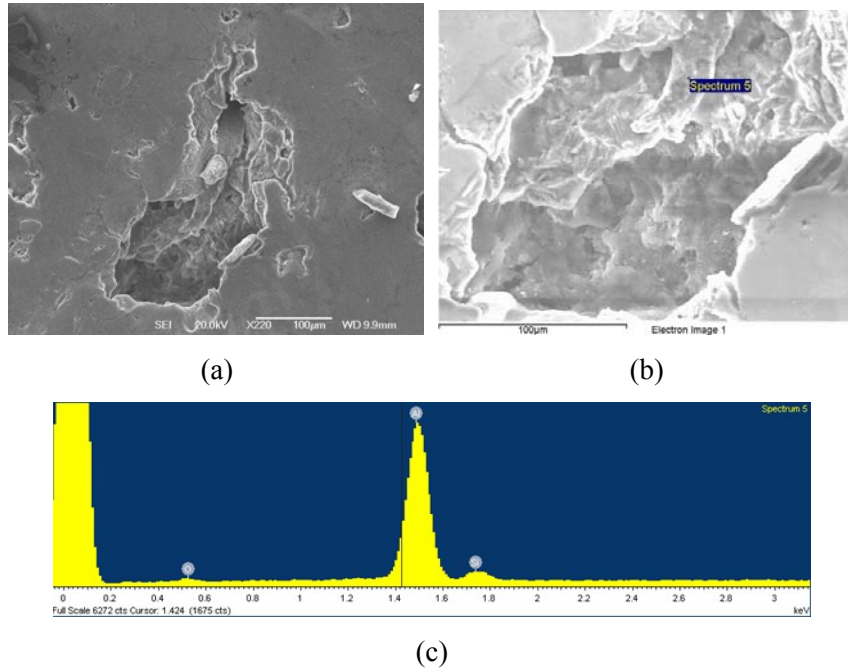


Figure 4.24: Different magnification SEM images of a re-melting specimen (a) and (b); (c) represents the EDS results of O_2 (10.82 wt%), Al (76 wt%), and Si (12.54 wt%)

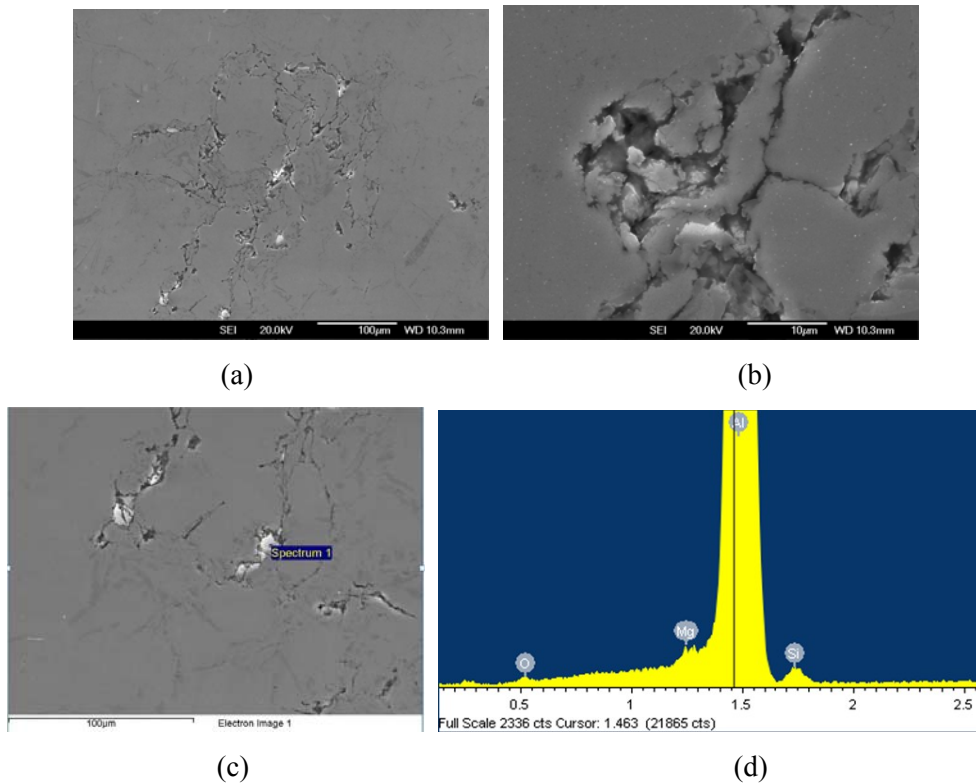


Figure 4.25: (a) and (b) SEM images of the defect in a polished metallographic section, (c) intermetallics and (d) EDS result.

Chapter 5

Discussion of Results

5.1 Technique for Developing Oxide Films Inside a Mould

A ‘furling’ process inside the mould is required to produce tangled bifilms in cast specimens [4]. The amount of surface turbulence in the mould is an important factor in generating and driving this furling process. In this experiment, an oxide generator, which could produce a hydraulic jump inside the mould, was used to generate surface turbulence. A 2-mm-deep section in the runner generated a liquid stream that was sufficiently fast and shallow to produce a hydraulic jump that generated surface turbulence. In addition, back flow helped increase the surface area in contact with air inside the mould (Figures 4.1(d) and (e)). The aluminium oxide films could be generated in milliseconds [4]; during back flow, almost all of the surface area that contacted air might be expected to produce oxide films.

The SEM and EDS results confirmed the presence of young oxides that were generated inside the mould. The thick, ‘crusty’ and unwrinkled shape of the oxides, the intermetallics and the relatively high weight-percentage of oxygen in the oxide (30–40 wt%) in the ingot specimen supports the conclusion that these oxides were old oxides. If there had been similar old oxides and intermetallics in the casting specimens, then it would have been clear that the oxides were not produced inside the mould. Based on the fracture surfaces that occurred during machining, both in the castings and after re-melting the specimens, the non-ingot specimens,

in comparison to oxides from the ingot, had thinner and more wrinkled oxide surfaces with complex 3-D geometry networks. In addition, the EDS results showed that the oxide content ranged from 5 wt% to 12 wt%, while the old oxides measured 30 wt% to 40 wt%, which supports the hypothesis that the oxides in the casting specimens were bifilms that had been produced during mould filling. The absence of old oxides in the cast specimens also indicates that the incorporation of a ceramic foam filter in the running system was an effective means of removing old oxides, as reported previously by Lai [80].

The oxide-developing technique (i.e. using an oxide generator in the gating system) worked in this experiment, which provides evidence of young oxides in casting specimens. According to Tables 4.5 and 4.6, the defect volume ratio was higher in casting specimens than re-melted specimens; therefore, this result also demonstrates that the defects inside specimens were not generated during the re-melting process.

5.2 Techniques for Applying X-ray Microtomography

5.2.1 Scanning Parameter

To obtain detailed descriptions of the aluminium porosity associated with bifilms, it is necessary to determine the smallest voxel size free from noise. The specimen must be at the centre of its holder. It is important to use cylindrical specimens with the smallest radius in order to acquire the smallest voxel size without noise signals.

The thickness of a thin aluminium oxide layer is approximately 3–4 nm (Storaska and Howe)

[81]. Therefore the film itself cannot be resolved, but merely the gap between bifilms. For this reason, it is important to use the smallest resolution possible in order to obtain a detailed description of the bifilm shape. The size of specimens significantly affects the spatial resolution in micro X-ray tomography scanning because the highest magnification produces the highest resolution and the most detailed images (Cooper et al.) [71].

This experiment also demonstrated that the resolution is limited by the size of the specimen. As the size of the specimen decreases, it becomes more likely that it will remain in the field of view (FOV) when increasing the magnification. Lower resolutions, however, produce more blurring and less sharp material edges. Nevertheless, the best resolution possible is important to observe bifilms with the best detail. Table 4.1 shows that the minimum spatial resolution is dependent on the diameter of the specimen. When the size of the specimens was decreased, the spatial resolution increased. In addition, as Table 4.1 shows, 3-mm and 4-mm diameter specimens achieved the same resolutions in this experiment. Some parts of the 3-mm diameter specimens, with ± 0.2 mm differences caused by machining error, could not fit into the FOV during magnification. To observe the entire specimen, the level of magnification had to be reduced and the 3-mm diameter specimen had to be treated like the 4-mm diameter specimen. The 3-mm diameter specimen, however, also had fracture problems during machining. The defects inside casting specimens initiated fractures during machining, as presented in Figures 4.11 and 4.12; the normal brittle fractures through the Si eutectic phase could be observed growing from the pores or defects to the edge of the specimen. These figures show that the fractures in specimens were caused by defects inside the specimens. Therefore, the 4-mm diameter specimen size is a reasonable machining size, and such a specimen still attains the highest spatial resolution: 5 $\mu\text{m}/\text{voxel}$.

The maximum exposure time and the smallest step angle are required to minimize noise and obtain detailed images. Short exposure times, such as a two-second exposure, can cause significant noise problems in aluminium specimens, as portrayed in Figure 4.13. The volume also decreased the noise signals in proportion to an increase in the exposure time (Table 4.2). Increasing the exposure time, however, had only a limited effect on improving the noise signals. Decreasing the rotation step angle also helped to reduce noise signals and improve the detail of defect shapes. A comparison of Figure 4.14 and Table 4.2 reveals that a small rotation step angle results in clear images with higher volumes, compared to the 7-second exposure time and 0.90 degree rotation angle. This means the smaller rotation step angle allows for more detailed descriptions of the targeted specimen area. Unlike decreasing the exposure time, however, decreasing the rotation step angle resulted in more data files and an increase in the scanning time. For example, changing from a 0.90 degree rotation step angle to a 0.45 degree rotation angle doubled both the number of files and the scanning time. Increasing the rotation step angle doubled the reconstruction time. Therefore, techniques to adjust the exposure time and rotation step angle can help minimize noise signals and make scanning more efficient.

5.2.2 Reconstruction parameter

The hardening artefact, which was caused by different characteristics of low-energy and high-energy photons, generated an image of the specimen that was denser at its edges than at its centre. In this study, a 1-mm aluminium filter was used. However, minor hardening artefacts were seen, which affected the volumetric analysis. In order to reduce these hardening artefacts, hardening correction was used to reduce the density of the image, which

correspondingly reduced its gray code level. There was a volume change in response to the hardening correction. As seen in Table 4.3, a correction level of 0–20 increased the volume to 0.055 mm^2 , with this increase in volume rapidly increasing after a correction level of 20. Therefore, hardening correction can be used, if necessary, but not at a correction level higher than level 20. The hardening correction level also reduced the density of images in the centre (Figure 4.15). Therefore, hardening correction significantly affects the volumetric data for surface-connected defects, especially in the targeted object, which is near the surface area of a specimen.

Ring artefacts, which were caused by defects in the scanning equipment or by a wrong specimen position on the specimen holder, could easily be seen in the scanned images. Ring artefact correction is based on the concept that the average intensity value of each concentric annulus can be removed from the pixels of the scanned image [82]. Increasing the ring artefact correction level helps reduce a ring artefact without any damage to the original image (Figure 4.16). Increasing the accuracy of ring artefact correction, however, leads to an increase in the reconstruction time.

5.2.3 Volumetric Imaging

The influence of the threshold is significant when building a 3-D volumetric image. The detail and volumetric data can change based on the threshold level and the 3-D volumetric image. The volumetric data and the image detail can increase as the threshold level increases (see Table 4.4). If the threshold level is too high, the 3-D image-building program includes the noise as part of the structure of the target object. At a threshold level of 130, the volume

rapidly increased from 0.024 to 0.19 mm³ because noisy signals were picked up (Table 4.4). If the threshold level is too low, however, then the volume of the targeted object and detailed shape descriptions will decrease.

The threshold level also affects the resolved defect structure of the 3-D image. Thin oxide defect structures were observed inside the selected area (the blue line indicates the defect area in Figures 4.17(a) and (c)). The thin section displayed a different intensity than that of the aluminium specimen body's. In addition, since the thickness of the oxide structures was less than the spatial resolution of 5 µm, the structures in the images may be responsible for the blurring of the images. The 3-D image-building program recognized the thin structures in the defects as empty space, as shown in Figures 4.18(b) and (d). Before building a 3-D image, it is important to make a decision regarding the defect range, which means either including the thin oxide structures (only air gaps) or excluding them as defects.

Issues were encountered in generating 3-D images of the pores associated with oxides, as shown in Figures 4.7 and 4.25, because the oxide was thinner than 5 µm. Because the oxide films were so thin relative to the voxel size, they could not be resolved directly in the images or reconstruction, and only the gas layers separating the two defects could be resolved. Even when this was seen, the gas gap was often less than one voxel when seen in polished sections. Thus, the ability to resolve the defects was still limited. Thin oxide layers can be more sensitive to their environment, so the 'unfurling' effect was more likely to be observed. However, thinner oxide layers could not be constructed with the minimum spatial resolution of 5 µm. Therefore, it was impossible to build the 3-D structure of a thin oxide. However, this technique can still be used to build a structure consisting of pores and oxides.

5.3 Techniques for Re-melting Bifilms in the Specimens

To develop a re-melting technique, this experiment tested a sealed quartz glass tube containing argon gas and a ceramic mould in an open-air environment. Problems arose when using the quartz glass tube at 745 °C. The liquid aluminium was melted and wetted the heated glass tube. During this wetting period, SiO₂ particles were transferred from the heated glass tube into the liquid aluminium specimens (Figure 4.20). The quartz glass tube changed its internal shape from cylindrical to irregularly round. The specimens' irregular shapes reduced their scanning resolutions and generated noise signals.

In overcoming the problems associated with re-melting in the quartz tubes, the melting times in air posed a problem when using ceramic tubes. The liquid aluminium in a 5-mm diameter ceramic mould could easily react with and pick up hydrogen from the air. Although any effect is inconclusive at this early stage of developing the technique, Raiszadeh and Griffiths produced a model that suggests that dissolved hydrogen can substantially affect the rate of oxidation and at high enough levels lead to pore growth [7]. Therefore, changes in the melting times affected, not only the reaction time of the bifilms, but also the dissolved gas content. Based on the results of melting 4-mm diameter specimens with different melting times, more small gas pores with fully spherical shapes could be observed after a five-minute melting time (Figure 4.21). Therefore, in order to minimize hydrogen penetration into the liquid aluminium, re-melting needs to occur within five minutes. The shape of the specimens was determined by the 5-mm diameter ceramic mould. The specimens stood in the ceramic mould during the melting process. Gravity caused some of the liquid aluminium to settle to the bottom of the mould; as a result, the bottom of the mould had a diameter of 5 mm and the

top of the mould had a diameter of 4 mm. In addition, gravity produced banding in the centres of the specimens. Hence, some of the specimens were not straight. The changes in the diameters and shapes of the specimens generated noise signals and spatial resolutions ranging from 5 μm to 6 μm . Therefore, techniques for retaining the shape of the specimens need to be developed to facilitate better resolution after the re-melting process.

5.4 Bifilm Behaviours after the Re-melting Process

According to the defect volume ratio results shown in Tables 4.5 and 4.6, the specimens contained more pores associated with oxides before melting than after melting. The before-melting defect ratio was two to eleven times greater than the after-melting ratio. Therefore, despite the absorption of hydrogen, the defects were apparently changed or lost during the melting cycle.

A buoyancy motion calculation was applied in order to predict the changes in the defect ratio. Using Stoke's law, the velocity of the defect motion was calculated with $V_s = 2(\rho_a - \rho_{al})gR^2/9\mu$ and the distances travelled during the different melting times were calculated using a value for gravity of 9.81 m/s^2 , ρ_a (density of air) of 1.2 kg/m^3 , ρ_{al} (density of aluminium) of 2343.75 kg/m^3 at $750 \text{ }^\circ\text{C}$ and μ (viscosity of liquid aluminium) of $1.038 \text{ mPa}\cdot\text{s}$ at $750 \text{ }^\circ\text{C}$ [83, 84]. Additionally, it was assumed that the defect shape was spherical and that the diameter ($2R$) of the sphere was the longest defect length.

Table 5.1 The floating velocity and drag force of targeted bifilms and the fracture force of oxide films.

Specimen ID	Defect size (mm)	Velocity (m/s)	Force (N)	Maximum drag force (N)
4 mm sp1	1.22	-1.83	-2.18×10^{-5}	36.89
4 mm sp2	1.1	-1.51	-1.6×10^{-5}	40.91
4 mm sp3	1.347	-2.23	-2.94×10^{-5}	33.41
4 mm sp4	1.77	-3.85	-6.67×10^{-5}	25.42
4 mm sp5	1.3	-2.08	-2.64×10^{-5}	34.62
3 mm sp1	2.114	-5.50	-11.37×10^{-5}	21.29
5 mm sp1	2.216	-6.04	-13.09×10^{-5}	20.31

According to Table 5.1, if the buoyancy was the only motion, the defects would float on the top of the specimens within three seconds. Using the velocity of the defects, the drag forces from the equation $F_d = 6\pi\mu RV_s$ were also calculated, as presented in Table 5.1. These forces, however, did not reach the level of the force resulting from the hoop stress calculation, $P = \sigma t / R$, with a theoretical strength of 4 GPa for the oxide film and an oxide thickness (t) of 3 nm [81].

During this procedure, with the exception of the surface-connected defects, the defects targeted for measurement changed their locations. The targeted defects could not be identified on either the tops or bottoms of the specimens. Therefore, something caused the defects to change their shapes.

Unlike the defects in the specimens, the surface-connected defects displayed no significant changes. These defects were in exactly the same positions as prior to the re-melting process (Figure 4.23(d)), and their shapes and volume were not significantly altered (Figures 4.19(a)

and 4.24(a) and Tables 4.5 and 4.6). This indicated that there was a pinning or tethering effect due to the connection of the internal defect to the surface defects.

The surface-connected defects were thus open to the air, so were not prone to inflation by hydrogen precipitation. Likewise, there was no inflation of the surface connected bifilms due to internal shrinkage during solidification. Therefore, of the four mechanisms of bifilm straightening and inflation proposed by Campbell, only those of intermetallic nucleation and growth on the wetted back surface and the pushing of the films by dendrite growth had the potential to change the film morphology. The surface defects on the tops and bottoms of specimens locally changed their shapes by shrinkage (see Figure 4.23(e)), which further supports another of Campbell's proposed mechanisms.

Through observations of the bifilms before re-melting, as Campbell proposed, the phenomenon of furling during the filling process was observed using the X-ray microtomography technique (Figure 4.18). However, within the limited sample of defects that were imaged both before and after re-melting, evidence of bifilm unfurling and dendrite tip pushing was *not obtained*. If the dendrite pushing and consequential unfurling process proposed by Campbell occurred, both the internal and surface connected bifilms should have been affected during solidification. However, the shape of the surface connected bifilms was unchanged by re-melting. Similarly, despite the presence of iron in the alloy and the formation of iron intermetallics during solidification, the convoluted folded bifilm morphology did not undergo any significant change during re-solidification. Therefore, from the limited number of cases studied in this project, the dendrite pushing and intermetallic mechanisms suggested by Campbell have either minor or no effect on the unfurling process.

Unfortunately, the effect of hydrogen penetration on the unfurling process could not be observed in this experiment because it was hard to track the targeted bifilms after the re-melting process due to their substantial buoyancy and measurements were not made of the dissolved hydrogen content before initial casting nor after re-melting. Calculations by Riaszadeh and Griffiths (2008) suggested that a 5- μm -thick film may completely oxidize the internal trapped atmosphere in only seven seconds [85]. If this were the case, in these experiments the entire transformation (oxidation and nitridation) would have been completed during the initial solidification of the test bar castings. However, it was noted that if the hydrogen content of the gas film trapped between the bifilm was less than that of the liquid metal, the diffusion of hydrogen into the gap could lead to a delay in the closure via oxidation.

While the results obtained offer some insight into the morphological evolution of bifilms in liquid aluminium, we did not succeed in generating a large number of specimens from which measurements could be made. One way in which the frequent loss of bifilms during re-melting may be overcome in the future would be to cast a metal matrix composite, rather than a pure aluminium alloy. Particles with a density similar to that of the entrained bifilms might be used to restrict bifilm motion during re-melting. A candidate second phase is B_4C , with a density of 2.51 g/cm^3 [86], which has previously been processed and cast as a metal matrix composite [87].

Chapter 6

Conclusions

1. The oxide generator, which was a 2-mm deep channel in the gating system, could produce a high defect density in test bars poured in sand moulds. In addition, internal turbulence led to the furling of the thin young bifilms.
2. Specimen size, centring of the specimen in the field of view and magnification are important factors for obtaining the smallest spatial voxel size. A small specimen size can achieve a higher magnification because a small specimen is more likely to fit in the field of view. Under high magnification, placing a specimen in the centre of the specimen holder can help to increase the magnification because it makes it more likely to be in the field of view.
3. Using a longer scanning exposure time and a smaller rotation step angle can help researchers obtain more accurate data. When the exposure time during the scanning increases, the noise signal is reduced. The smaller rotation step angle not only reduces the noise signals but also allows for more detail descriptions. The optimum scanning conditions were found to be the minimum rotation step angle and the longest possible exposure time.
4. Adjusting the threshold level applied during volume reconstruction can affect the resolved morphology of 3-D structures. A higher threshold level allows for more detailed descriptions of 3-D structures but also generates greater noise signals.

5. When using the ceramic mould re-melting technique, it was difficult to control the pores associated with oxides inside specimens, but it was possible to observe surface-connected defects. Bifilm buoyancy effects resulted in floating to the upper specimen surface within a few seconds. Defects that floated to the tops of specimens suffered from shrinkage, so it was not possible to differentiate the targeted bifilms from the shrinkage. Surface-connected defects retained their original positions.
6. Surface connected defects were not prone to hydrogen precipitation or shrinkage driven inflation. However, the remaining mechanisms of dendrite pushing and intermetallic growth could not be seen to produce any unfurling effect on the surface connected defects. Therefore, dendrite pushing and intermetallic growth have either minor or no effect on bifilm defects.

Chapter 7

Future Work

1. Using spatial voxels that are as small as possible is an important factor in this X-ray tomography technique for obtaining detailed information without noise signals. Skyscan 1072 can achieve a spatial resolution of less than 3 μm , if the specimen size can be reduced to less than 3 mm. A laser or plasma-cutting machine may be suitable for the preparation of specimens smaller than 4 mm in diameter.
2. Using the ceramic re-melting technique led to bifilm motion and precluded a determination of a specimen's position after re-melting. To solve this problem, local heating techniques such as equipment that can heat an area with dimensions smaller than 2 mm might help to reduce the possibility of losing the position.
3. Degassing with different hydrogen levels in the liquid aluminium would help prove the hydrogen-penetration effect during holding and solidification that Campbell proposed and Raiszadeh and Griffiths (2008) calculated. If the hydrogen affects the unfurling, then different hydrogen levels will show different levels of unfurling.
4. It would also be good to conduct tests using different levels of iron in the aluminium alloy. In this experiment, the iron level was low, so the effect of iron intermetallics was minor. Experimenting with different levels of iron content would facilitate understanding the relationship between intermetallics and the unfurling effect.
5. For a more accurate measurement of the volume of targeted objects, a program called Amira should be used. The programs used in this experiment, such as the programs from Skyscan and the Voxel Counter Function in the image J program, require untrimmed reconstructed images. Thus, some results contained noise signals and other

defects in the region of interest (ROI). Amira, however, uses 3-D imaging, which can trim images before measuring targeted objects. Therefore, the morphology data result would be more accurate.

6. Using Synchrotron microCT would be another challenge for obtaining detailed morphology information. In this experiment, the maximum spatial resolution reached 5 μm , which was still larger than 3–4 μm . The synchrotron microCT, however, can reach smaller spatial resolutions, even as small as 0.3 μm voxels. This ability would facilitate the observation of more detailed defect shapes.

References

- [1] G. K. Sigworth, 'A Scientific Basis for Degassing Aluminum', *AFS Transactions*, vol. 81, 1987.
- [2] B. P. Cochran, M. L. Fenyves, J. L. Jeanneret, and R. P. Mulac, 'Flux practice in Aluminum Melting', *AFS Transactions*, vol. 88, 1992.
- [3] A. S. o. Metals, *Metals Handbook* vol. 15. Metals Park, OH, 1988.
- [4] J. Campbell, 'Entrainment defects', *Materials Science and Technology*, vol. 22, pp. 127-145, Feb 2006.
- [5] F. Bahreinian, S. M. A. Boutorabi, and J. Campbell, 'Critical gate velocity for magnesium casting alloy (ZK51A)', *International Journal of Cast Metals Research*, vol. 19, pp. 45-51, 2006.
- [6] J. Campbell, *Castings*, 2nd ed. Oxford; Boston: Butterworth Heinemann, 2003.
- [7] R. Raiszadeh and W. D. Griffiths, 'A method to study the history of a double oxide film defect in liquid aluminum alloys', *Metallurgical and Materials Transactions B-Process Metallurgy and Materials Processing Science*, vol. 37, pp. 865-871, Dec 2006.
- [8] A. O. Omotunde, 'Effect of Time on Oxide Film Defects in Aluminium Alloy Casting', in *School of Metallurgy and Materials*. vol. Master of Philosophy Birmingham: University of Birmingham, 2006, p. 108.
- [9] X. Cao and J. Campbell, 'Oxide inclusion defects in Al-Si-Mg cast alloys', *Canadian Metallurgical Quarterly*, vol. 44, pp. 435-447, Oct 2005.
- [10] P. Tafforeau, R. Boistel, E. Boller, A. Bravin, M. Brunet, Y. Chaimanee, P. Cloetens, M. Feist, J. Hozowska, J. Jaeger, R. F. Kay, V. Lassari, L. Marivaux, A. Nel, C. Nemoz, X. Thibault, P. Vignaud, and S. Zabler, 'Applications of X-ray synchrotron microtomography for non-destructive 3D Studies of paleontological specimens,' *Applied Physics A*, vol. 83, 2006.
- [11] R. A. Ketcham and W. D. Carlson, 'Acquisition, optimization and interpretation of X-ray computed tomographic imagery: applications to the geosciences', *Computers & Geosciences*, vol. 27, pp. 381-400, May 2001.
- [12] R. Holmstad, A. Goel, S. Ramaswamy, and Gregersen, 'Visualization and characterization of high resolution 3D images of paper samples', *Appita Journal* vol. 59, September 2006.
- [13] E. Maire, J. Y. Buffiere, L. Salvo, J. J. Blandin, W. Ludwig, and J. M. Letang, 'On the application of X-ray microtomography in the field of materials science', *Advanced Engineering Materials*, vol. 3, pp. 539-546, Aug 2001.
- [14] C. F. Martin, C. Josserond, L. Salvo, J. J. Blandin, P. Cloetens, and E. Boller, 'Characterisation by X-ray Micro-Tomography of Cavity Coalescence during superplastic deformation', *Scripta Materialia*, vol. 42, 2000.
- [15] E. Maire, J. Y. Buffiere, R. Mokso, P. Cloetens, and W. Ludwig, 'Non destructive three dimensional imaging of aluminum alloys', *Aluminium Alloys 2006, Pts 1 and 2*, vol. 519-521, pp. 1367-1372, 2006.
- [16] L. Qian, H. Toda, K. Uesugi, T. Ohgaki, M. Kobayashi, and T. Kobayashi, 'Three-dimensional Visualization of ductile fracture in an Al-Si alloy by high resolution synchrotron X-ray microtomography', *Materials science and Engineering A*, vol. 483-484, 2008.

- [17] S. Y. Oh, J. A. Cornie, and K. C. Russell, 'Wetting of Ceramic Particulates with Liquid Aluminum-Alloys .2. Study of Wettability', *Metallurgical Transactions a-Physical Metallurgy and Materials Science*, vol. 20, pp. 533-541, Mar 1989.
- [18] V. Laurent, D. Chatain, C. Chatillon, and N. Eustathopoulos, 'Wettability of Monocrystalline Alumina by Aluminum between Its Melting-Point and 1273-K', *Acta Metallurgica*, vol. 36, pp. 1797-1803, Jul 1988.
- [19] J. J. Brennan and J. A. Pask, 'Effect of Nature of Surfaces on Wetting of Sapphire by Liquid Aluminum,' *Journal of the American Ceramic Society*, vol. 51, pp. 569-&, 1968.
- [20] H. J. Mathieu, M. Datta, and D. Landolt, 'Thickness of Natural Oxide-Films Determined by Aes and Xps with without Sputtering', *Journal of Vacuum Science & Technology a-Vacuum Surfaces and Films*, vol. 3, pp. 331-335, 1985.
- [21] L. P. H. Jeurgens, W. G. Sloof, F. D. Tichelaar, and E. J. Mittemeijer, 'Structure and morphology of aluminium-oxide films formed by thermal oxidation of aluminium', *Thin Solid Films*, vol. 418, pp. 89-101, Oct 15 2002.
- [22] S. S. Impey and D. J. NICHOLLS Jr., 'A study of the effect of magnesium additions on the oxide-growth morphologies on liquid aluminium alloys', in *1st International Conf on the Microscopy of Oxidation*, L. G. BENNETT MJ, Ed., Selwyn College, Cambridge, England: Inst. Metals, London, 1992, pp. 238-244.
- [23] C. N. Cochran, D. L. Belitskus, and D. L. Kinosz, 'Oxidation of Aluminum-Magnesium Melts in Air, Oxygen, Flue-Gas, and Carbon-Dioxide', *Metallurgical Transactions B-Process Metallurgy*, vol. 8, pp. 323-332, 1977.
- [24] L. P. H. Jeurgens, W. G. Sloof, F. D. Tichelaar, and E. J. Mittemeijer, 'Thermodynamic stability of amorphous oxide films on metals: Application to aluminum oxide films on aluminum substrates', *Physical Review B*, vol. 62, pp. 4707-4719, Aug 15 2000.
- [25] C. W. M. Nyahumwa, 'Influence of Oxide Film Filling Defects on Fatigue Properties of Casting Al-7Si-Mg Alloy', in *School of Metallurgy and Materials* vol. Doctor of Philosophy Birmingham University of Birmingham 1997, p. 122.
- [26] Q. G. Wang, C. J. Davidson, J. R. Griffiths, and P. N. Crepeau, 'Oxide films, pores and the fatigue lives of cast aluminum alloys', *Metallurgical and Materials Transactions B-Process Metallurgy and Materials Processing Science*, vol. 37, pp. 887-895, Dec 2006.
- [27] C. Nyahumwa, N. R. Green, and J. Campbell, 'Influence of casting technique and hot isostatic pressing on the fatigue of an Al-7Si-Mg alloy', *Metallurgical and Materials Transactions a-Physical Metallurgy and Materials Science*, vol. 32, pp. 349-358, Feb 2001.
- [28] C. Nyahumwa, N. Green, and J. Campbell, 'Effect of mold-filling turbulence on fatigue properties of casting aluminum alloys', *Transactions of The American Foundrymen's Society* vol. 106, 1998.
- [29] J. Runyoro and J. Campbell, 'Critical gate velocities for Film-Forming Casting Alloys: A basis for process specification', *Transactions of The American Foundrymen's Society* vol. 37, 1992.
- [30] J. Campbell, *Castings Practice*, 2004.
- [31] J. Campbell, 'An Overview of the Effects of Bifilms on the structure and Properties of Cast Alloys', *Metallurgical and Materials Transactions B-Physical Metallurgy and Materials Science*, vol. 37B, pp. 857-863, 2006.

- [32] C. Nyahumwa, 'Influence of Oxide Film Filling Defects on Fatigue Properties of Cast Al-7Si-Mg Alloy', in *Metallurgy and Materials*. vol. Doctor of Philosophy Birmingham: University of Birmingham, 1997, p. 121.
- [33] J. M. Boileau, 'An Examination Of Inclusions In A Quiescent Metal Furnace', in *6th International AFS Conference: Molten Aluminum Processing*. vol. 3 Orlando, FL, USA: American Foundry Society, 2001, p. 1.
- [34] C. E. Ransley and H. Neufeld, 'The Solubility of Hydrogen in Liquid and Solid Aluminium', *Journal of the Institute of Metals*, vol. 74, pp. 599-620, 1948.
- [35] P. N. Anyalebechi, 'Analysis of the Effects of Alloying Elements on Hydrogen Solubility in Liquid Aluminum-Alloys', *Scripta Metallurgica Et Materialia*, vol. 33, pp. 1209-1216, Oct 15 1995.
- [36] P. S. Mohanty, F. H. Samuel, and J. E. Gruzleski, 'Experimental Study on Pore Nucleation by Inclusions in aluminum Castings', *Transactions of The American Foundrymen's Society* vol. 27, 1995.
- [37] S. Saikawa, K. Nakai, Y. Sugiura, and A. Kamio, 'Effect of hydrogen gas content on generation of porosity in Al-Li casting alloys', *Materials Transactions Jim*, vol. 40, pp. 57-63, Jan 1999.
- [38] G. A. Young and J. R. Scully, 'The diffusion and trapping of hydrogen in high purity aluminum', *Acta Materialia*, vol. 46, pp. 6337-6349, Nov 20 1998.
- [39] G. K. Sigworth and D. Apelian, 'The influence of Molten Metal Processing on Mechanical Properties of Casting Al-Si-Mg Alloys', *American Foundry Society Transactions*, vol. 139, pp. 811-823, 1989.
- [40] G. K. Sigworth, 'The modification of Al-Si casting alloys: important practical and theoretical aspects', *International Journal of Metalcasting*, pp. 19-41, Spring 2008 Spring 2008.
- [41] M. C. Flemings, *Solidification processing*. New York; London: McGraw-Hill, 1974.
- [42] F. H. Samuel, P. Ouellet, and A. Simard, 'Assessment of melt cleanliness and analysis of inclusions in Al-Si alloys using the Prefill pressure filtration technique', *International Journal of Cast Metals Research*, vol. 12, pp. 17-33, 1999.
- [43] X. Cao and J. Campbell, 'Effect of precipitation and sedimentation of primary alpha-Fe phase on liquid metal quality of cast Al-11 center dot 1Si-0 center dot 4Mg alloy', *International Journal of Cast Metals Research*, vol. 17, pp. 1-11, 2004.
- [44] X. Cao and J. Campbell, 'The nucleation of Fe-rich phases on oxide films in Al-11.5Si-0.4Mg cast alloys', *Metallurgical and Materials Transactions a-Physical Metallurgy and Materials Science*, vol. 34A, pp. 1409-1420, Jul 2003.
- [45] S. Fox and J. Campbell, 'Visualisation of oxide film defects during solidification of aluminium alloys', *Scripta Materialia*, vol. 43, pp. 881-886, Oct 30 2000.
- [46] S. Shivkumar, L. Wang, and D. Apelian, 'Molten Metal Processing of Advanced Cast Aluminum Alloys', *Jom-Journal of the Minerals Metals & Materials Society*, vol. 43, 1991.
- [47] X. G. Chen, F. J. Klinkenberg, R. Ellerbrok, and S. Engler, 'Efficiency of Impeller Degassing and Regassing Phenomena in Aluminum Melts', *Transactions of The American Foundrymen's Society*, vol. 94, 1994.
- [48] M. Maniruzzaman and M. Makhlof, 'Mathematical modeling and computer simulation of the rotating impeller particle flotation process: Part I. Fluid flow', *Metallurgical and Materials Transactions B-Process Metallurgy and Materials Processing Science*, vol. 33, pp. 297-303, Apr 2002.

- [49] X. Cao, 'Mechanisms of Pressure Filtration of Liquid Aluminum Alloys', *Metallurgical and Materials Transactions B-Physical Metallurgy and Materials Science*, vol. 37B, p. 1075, 2006.
- [50] R. P. Pishel, 'A Filter is More than just a Filter', in *Foundryman management & Technology* OH: Penton Meida Inc, 2003.
- [51] N. R. Green and J. Campbell, 'Influence of Oxide Film Filling Defects on the Strength of Al-7Si-Mg Alloy Castings', *AFS Transactions* vol. 114, 1994.
- [52] L. Liu and F. H. Samuel, 'Effect of inclusions on the tensile properties of Al-7% Si-0.35% Mg (A356.2) aluminium casting alloy', *Journal of Materials Science*, vol. 33, pp. 2269-2281, May 1 1998.
- [53] A. Rushton, A. S. Ward, and R. G. Holdich, *Solid liquid Separation Technology* Weinheim, Germany, 1996.
- [54] A. Prosch and B. Larson, 'Real-Time Radiography: An introductory Course Module for NDT Students', Northeast Iowa Community College and Iowa State University 2000.
- [55] I. M. Watt, *The principles and practice of electron microscopy*: Cambridge University Press, 1985.
- [56] S. R. Stock, 'X-ray microtomography of materials', *International Materials Reviews*, vol. 44, pp. 141-164, 1999.
- [57] S. R. Stock, 'Recent advances in X-ray microtomography applied to materials', *International Materials Reviews*, vol. 53, pp. 129-181, May 2008.
- [58] E. Maire, J. C. Grenier, D. Daniel, A. Baldacci, H. Klocker, and A. Bigot, 'Quantitative 3D characterization of intermetallic phases in an Al-Mg industrial alloy by X-ray microtomography', *Scripta Materialia*, vol. 55, pp. 123-126, Jul 2006.
- [59] G. van Kaick and S. Delorme, 'Computed tomography in various fields outside medicine', *European Radiology*, vol. 15, pp. D74-D81, Nov 2005.
- [60] J. Y. Buffiere, E. Maire, C. Verdu, P. Cloetens, M. Pateyron, G. Peix, and J. Baruchel, 'Damage assessment in an Al/SiC composite during monotonic tensile tests using synchrotron X-ray microtomography', *Materials Science and Engineering a-Structural Materials Properties Microstructure and Processing*, vol. 234, pp. 633-635, Aug 30 1997.
- [61] J. Y. Buffiere, S. Savelli, P. H. Jouneau, E. Maire, and R. Fougères, 'Experimental study of porosity and its relation to fatigue mechanisms of model Al-Si7-Mg0.3 cast Al alloys', *Materials Science and Engineering a-Structural Materials Properties Microstructure and Processing*, vol. 316, pp. 115-126, Oct 15 2001.
- [62] E. Maire, C. Bordreuil, L. Babout, and J. C. Boyer, 'Damage initiation and growth in metals. Comparison between modelling and tomography experiments', *Journal of the Mechanics and Physics of Solids*, vol. 53, pp. 2411-2434, Nov 2005.
- [63] E. Maire, J. C. Grenier, and L. Babout, 'Damage investigation in aluminum alloys by X ray tomography', *Aluminium Alloys 2006, Pts 1 and 2*, vol. 519-521, pp. 821-827, 2006.
- [64] A. Prasad, H. Henein, E. Maire, and C. A. Gandin, 'Understanding the rapid solidification of Al-4.3Cu and Al-17Cu using X-ray tomography', *Metallurgical and Materials Transactions a-Physical Metallurgy and Materials Science*, vol. 37A, pp. 249-257, Jan 2006.

- [65] O. Betz, U. Wegst, D. Weide, M. Heethoff, L. Helfen, W. K. Lee, and P. Cloetens, 'Imaging applications of synchrotron X-ray phase-contrast microtomography in biological morphology and biomaterials science. 1. General aspects of the technique and its advantages in the analysis of millimetre-sized arthropod structure', *Journal of Microscopy-Oxford*, vol. 227, pp. 51-71, Jul 2007.
- [66] B. P. Flannery, H. W. Deckman, W. G. Roberge, and K. L. Damico, '3-Dimensional X-Ray Microtomography', *Science*, vol. 237, pp. 1439-1444, Sep 18 1987.
- [67] K. Remeysen and R. Swennen, 'Application of microfocus computed tomography in carbonate reservoir characterization: Possibilities and limitations', *Marine and Petroleum Geology*, vol. 25, pp. 486-499, Jun 2008.
- [68] S. E. Umbaugh, *Computer vision and image processing: a practical approach using CVIPtools*. Englewood Cliffs, N.J.: Prentice Hall PTR, 1998.
- [69] G. Lohmann, *Volumetric image analysis*. Chichester: Stuttgart: Wiley; Teubner, 1998.
- [70] G. R. Davis and J. C. Elliott, 'Artefacts in X-ray microtomography of materials', *Materials Science and Technology*, vol. 22, pp. 1011-1018, Sep 2006.
- [71] D. Cooper, A. Turinsky, C. Sensen, and B. Hallgrimsson, 'Effect of voxel size on 3D micro-CT analysis of cortical bone porosity', *Calcified Tissue International*, vol. 80, pp. 211-219, Mar 2007.
- [72] Skyscan, *Sky Scan 1072-Instruction Manual*, 3rd ed. Aartselaar: Skyscan n.v., 1998.
- [73] D. Wildenschild, J. W. Hopmans, C. M. P. Vaz, M. L. Rivers, D. Rikard, and B. S. B. Christensen, 'Using X-ray computed tomography in hydrology: systems, resolutions, and limitations', *Journal of Hydrology*, vol. 267, pp. 285-297, Oct 15 2002.
- [74] J. F. Barrett and N. Keat, 'Artifacts in CT: Recognition and avoidance', *Radiographics*, vol. 24, pp. 1679-1691, Nov-Dec 2004.
- [75] B. R. Munson, D. F. Young, and T. H. Okiishi, *Fundamentals of fluid mechanics*, 4th ed. New York, N.Y.: John Wiley & Sons, 2002.
- [76] M. Cox, R. A. Harding, and J. Campbell, 'Optimised running system design for bottom filled aluminium alloy 2L99 investment castings', *Materials Science and Technology*, vol. 19, pp. 613-625, May 2003.
- [77] G. Calleja, 'Influence of Mineralogy on Petrophysical Properties of Petroleum Reservoir Beds', in *School of Biological, Earth and Environmental Sciences*. vol. Mater of Science in Applied Geology Sydney: University of new South Wales, 2005, pp. 129 - 245.
- [78] S. Jones, 'Improved Investment Casting Process', 2004.
- [80] N.-W. Lai, 'The Critical Ingate Velocity in Mg and Al Alloys', in *Metallurgy and Materials*. vol. Doctor of Philosophy Birmingham: University of Birmingham, 2004.
- [81] G. A. Storaska and J. M. Howe, 'In-situ transmission electron microscopy investigation of surface-oxide, stress-relief mechanisms during melting of sub-micrometer Al-Si alloy particles', *Materials Science and Engineering a-Structural Materials Properties Microstructure and Processing*, vol. 368, pp. 183-190, Mar 15 2004.
- [82] D. A. Freundlich, 'Ring artefact correction for computerized tomography', U.S. Patent, Ed. USA: Elscint, Inc, 1986.
- [83] J. E. Hatch, *Aluminum: properties and physical metallurgy*: American Society for Metals International, 1984.
- [84] H. Lamb, *Hydrodynamics*, 6th ed.: Cambridge University press, 1994.

- [85] R. Raiszadeh and W. D. Griffiths, 'A semi-empirical mathematical model to estimate the duration of the atmosphere within a double oxide film defect in pure aluminum alloy', *Metallurgical and Materials Transactions B-Process Metallurgy and Materials Processing Science*, vol. 39, pp. 298-303, Apr 2008.
- [86] C. J. Smithells, E. A. Brandes, and G. Brook, *Smithell's metal reference book*, 7th ed. ed.: Butterworths, 1991.
- [87] B. Previtali, D. Poggi, and c. Taccardo, 'Application of traditional investment casting process to aluminium matrix composites', *Composites*, vol. Part A 39, p. 12, 2008.